# J|A|C|S

## A R T I C L E S

# Redox Non-innocence of Thioether Macrocycles: Elucidation of the Electronic Structures of Mononuclear Complexes of Gold(II) and Silver(II)

Jennifer L. Shaw,[†] Joanna Wolowska,[‡] David Collison,[‡] Judith A. K. Howard,[§]
Eric J. L. McInnes,*,[‡] Jonathan McMaster,*,[†] Alexander J. Blake,[†]
Claire Wilson,[†] and Martin Schröder*,[†]

*Contribution from the School of Chemistry, University of Nottingham, Nottingham NG7 2RD,
United Kingdom, EPSRC Multi-Frequency EPR Centre, School of Chemistry, University of
Manchester, Manchester M13 9PL, United Kingdom, and Department of Chemistry,
University of Durham, Durham DH1 3LE, United Kingdom*

Received May 24, 2006; E-mail: M.Schroder@nottingham.ac.uk

***Abstract:*** The mononuclear +2 oxidation state metal complexes $[Au([9]aneS_3)_2]^{2+}$ and $[Ag([18]aneS_6)]^{2+}$ have been synthesized and characterized crystallographically. The crystal structure of the Au(II) species $[Au([9]aneS_3)_2](BF_4)_2$ shows a Jahn−Teller tetragonally distorted geometry with Au−S(1) = 2.839(5), Au−S(2) = 2.462(5), and Au−S(3) = 2.452(5) Å. The related Ag(II) complex $[Ag([18]aneS_6)](ClO_4)_2$ has been structurally characterized at both 150 and 30 K and is the first structurally characterized complex of Ag(II) with homoleptic thioether S-coordination. The single-crystal X-ray structure of $[Ag([18]aneS_6)](ClO_4)_2$ confirms octahedral homoleptic $S_6$-thioether coordination. At 150 K, the structure contains two independent Ag(II)−S distances of 2.569(7) and 2.720(6) Å. At 30 K, the structure retains two independent Ag(II)−S distances of 2.615(6) and 2.620(6) Å, with the complex cation retaining 3-fold symmetry. The electronic structures of $[Au([9]aneS_3)_2]^{2+}$ and $[Ag([18]aneS_6)]^{2+}$ have been probed in depth using multifrequency EPR spectroscopy coupled with DFT calculations. For $[Au([9]aneS_3)_2]^{2+}$, the spectra are complex due to large quadrupole coupling to [197]Au. Simulation of the multifrequency spectra gives the principal *g* values, hyperfine (*A*) and quadrupole (*P*) couplings, and furthermore reveals non-co-incidence of the principal axes of the *P* tensor with respect to the *A* and *g* matrices. These results are rationalized in terms of the electronic and geometric structure and reveal that the SOMO has *ca.* 30% Au $5d_{xy}$ character, consistent with DFT calculations (27% Au character). For $[Ag([18]aneS_6)]^{2+}$, detailed EPR spectroscopic analysis confirms that the SOMO has *ca.* 26% Ag $4d_{xy}$ character and DFT calculations are consistent with this result (22% Ag character).

## Introduction

The common oxidation states for gold and silver (M) are +1 and +3 with paramagnetic, mononuclear d[9] M(II) complexes being especially rare. Many of the reported formal M(II) mononuclear species are often better described as ligand-radical species with delocalisation of the unpaired electron into ligand orbitals,[1,2] while the formation of diamagnetic M(II)−M(II) bonded species, for example via oxidative addition of halogens to binuclear Au(I) derivatives, is also common.[3]

**Gold:** Genuine mononuclear Au(II) compounds are rare. Examples include the first metal−Xe compound, $[AuXe_4]$-$(Sb_2F_{11})_2$, obtained by reduction of $AuX_3$ with elemental Xe,[4] and $[AuXe_2][Sb_2F_{11}]_2$ in which the Au(II) ion has an octahedral

coordination geometry.[5] A series of EPR studies on Au(II) complexes of thiocarbamates,[6] maleonitriledithiolates,[7] dimercaptoisotrithione,[1] *o*-methylthioaniline, and *N*-(2-pyridylmethyl)-2-mercaptoaniline[8] have been reported. The structure of the formal Au(II) complex $(^nBu_4N)_2[Au(mnt)_2]$ (mnt = maleonitriledithiolate), obtained as a green, air-sensitive product by reaction of the Au(III) species, $^nBu_4N[Au^{III}(mnt)_2]$, with one equivalent of $^nBu_4N[BH_4]$, shows[9] the Au center bound to four S donors in a square-planar geometry with all Au−S bond lengths equivalent [Au−S = 2.4156(7) Å]. Detailed EPR[10] and ENDOR[2] spectroscopic studies on $(^nBu_4N)_2[Au(mnt)_2]$ in

† University of Nottingham.
‡ University of Manchester.
§ University of Durham.
(1) Ihlo, L.; Olk, R.-M.; Kirmse, R. *Inorg. Chem. Commun.* **2001**, *4*, 626−628.
(2) Ihlo, L.; Olk, R.-M.; Böttcher, R.; Kirmse, R. *Inorg. Chim. Acta.* **1998**, *281*, 160−164.
(3) Laguna, A.; Laguna, M. *Coord. Chem. Rev.* **1999**, *193−195*, 837−856.
(4) Elder, S. H.; Lucier, G. M.; Hollander, F. J.; Bartlett, N. *J. Am. Chem. Soc.* **1997**, *119*, 1020−1026.

(5) (a) Siedel, S.; Seppelt, K. *Science* **2000**, *290*, 117−118; (b) Drews, T.; Siedel, S.; Seppelt, K. *Angew. Chem., Int. Ed.* **2002**, *41*, 454−456.
(6) (a) Vänngård, T.; Åkerström, S. *Nature* **1959**, *184*, 183−184. (b) van Willigen, H; van Rens, J. G. M. *Chem. Phys. Lett.* **1968**, *2*, 283−285.
(7) (a) Waters, J. H.; Gray, H. B. *J. Am. Chem. Soc.* **1965**, *87*, 3534−3535. (b) van Rens, J. G. M; Viegers, M. P. A; de Boer, E. *Chem. Phys. Lett.* **1974**, *28*, 104−108. (c) Schlupp, R. L.; Maki, A. H. *Inorg. Chem.* **1974**, *13*, 44−51.
(8) Koley, A. P.; Prasad, L. S.; Manoharan, P. T.; Ghosh, S. *Inorg. Chim. Acta.* **1992**, *194*, 219−225.
(9) Kirmse, R.; Kampf, M.; Olk, R.-M.; Hildebrand, M.; Krautscheid, H. *Z. Anorg. Allg. Chem.* **2004**, *630*, 1433−1436.
(10) Ihlo, L.; Stösser, R.; Hofbauer, W.; Böttcher, R.; Kirmse, R. *Z. Naturforsch.* **1999**, *54b*, 597−602.

($^n$Bu$_4$N)$_2$[Ni$^{II}$(mnt)$_2$] as a diamagnetic host gave spin-Hamilton parameters $g_x = 1.985$, $g_y = 2.005$, $g_z = 2.016$, $A_x = -39.6$, $A_y = -40.4$, $A_z = -41.2$ K. These data, together with extended Hückel theory molecular orbital calculations, confirmed that in ($^n$Bu$_4$N)$_2$[Au(mnt)$_2$] *ca.* 60% of the unpaired electron density within the singly occupied molecular orbital (SOMO) is localized on the S donors and only *ca.* 8% localized on the Au center.[2] More recently, a stable, monomeric Au(II) complex has been reported with hematoporphyrin,[11] in which the six-coordinate Au center is bound to the hematoporphyrin macro-cycle and two water molecules are coordinated axially. The EPR spectrum of this complex is dominated by an intense signal attributed to a stable free radical; a less intense signal containing nine lines due to the interaction of the unpaired electron with the four coordinated N atoms is also observed.

**Silver:** Mononuclear, paramagnetic Ag(II) centers are more common than the analogous Au(II) species, but 2+ can still be regarded as an unusual oxidation state for silver. Ag(II) species have been identified in the processesing of radioactive waste at room temperature[12] and are known as effective oxidants for organic substrates.[13−15] The complexes of formal Ag(II) centers are dominated by porphyrin[16] and aza macrocyclic[17] species in which the Ag(II) center is coordinated to all four N-donors of the ligand in a square planar geometry with potential weak axial interaction(s) to counter-anions or co-ligands. Highly oxidizing Ag(II) products containing N-heterocyclic ligands can be prepared via oxidation of precursor Ag(I) complexes using PbO$_2$, BaO$_2$, CaO$_2$, or O$_3$.[15,18−20] Many of these formal Ag(II) complexes have been studied by EPR spectroscopy[19,21] including complexes of dialkyldithiocarbamates that show a doublet with hyperfine splittings to $^{107}$Ag and $^{109}$Ag, with $g_{iso} = 2.019$ and $A_{iso} = 27 \times 10^{-4}$ cm$^{-1}$. Doublet spectra are also observed in the fluid solution EPR spectrum of [Ag(mnt)$_2$]$^{2-}$ (mnt$^{2-}$ = maleonitriledithiolate) with $g_{iso} = 2.019$, $A_{iso} = 31.4$ G.[22]

Manoharan and Kundu have reported a study on Jahn−Teller distortions in the Ag(II) complex of 1,8-diammonio-3,6,10,13,-16,19 hexaaza-bicyclo[6.6.6]icosane in which the Ag center is bound to six N-donors of the cryptand.[23] Single-crystal EPR measurements reveal a dynamic Jahn−Teller distortion above 230 K, a static Jahn−Teller distortion between 230 and 120 K, and below 110 K evidence of exchange interactions;[23] X-band measurements on a single crystal at room-temperature gave $g_1 = 2.052$, $g_2 = 2.078$ and $g_3 = 2.086$. Ag(II) selenocarbamates show g values, for example for [Ag(dsc)$_2$] (dsc = diselenocar-bamate), that are close to that for the free electron.[19] Kirmse et al. have studied bis(di-*n*-butyldiselenocarbamate)silver(II) in a diamagnetic palladium(II) host by single-crystal EPR spectroscopy.[24] The spectra obtained were rhombic with hyperfine splitting to $^{107}$Ag and $^{109}$Ag as well as to $^{77}$Se ($I = 1/2$, 7.5% natural abundance). The question of whether these are ligand-centered radicals remains relevant in the characterization and analysis of these complexes.

**Thioether Crowns:** As part of our studies on the stabilization of unusual oxidation states [Co(I),[25] Rh(II),[26] Ni(I),[27] Ni(III),[28] Pd(I),[29] Pd(III),[30] Pt(I),[31] and Pt(III)[32]] using macrocyclic ligands,[33] we report herein the first crystal structure of a homoleptic thioether S-bound Ag(II) complex, [Ag([18]aneS$_6$)]-(ClO$_4$)$_2$, together with a full multifrequency EPR spectroscopic analysis coupled to DFT calculations to interrogate the detailed electronic structure and nature of the SOMO in [Ag([18]-aneS$_6$)]$^{2+}$ and the related Au(II) species [Au([9]aneS$_3$)$_2$]$^{2+}$. We were first to report the single-crystal structure of [Au([9]-aneS$_3$)$_2$]$^{2+}$ in which the formal d$^9$ Au(II) center is bound to six S atoms of two [9]aneS$_3$ ligands in a Jahn−Teller distorted octahedral geometry with equatorial Au(II)−S distances of 2.452(5) and 2.462(5) Å and longer, apical Au(II)−S bonds at 2.839(5)Å.[34] The stabilization of other Au[34−36] and Ag[36−39]

(11) Gencheva, G.; Tsekova, D.; Gochev, G.; Mehandjiev, D.; Bontchev, P. R. *Inorg. Chem. Commun.* **2003**, *6*, 325−328.

(12) Farmer, C.; Wang, F. T.; Hawley-Fedder, R. A.; Lewis, P. R.; Summers, L. J.; Foiles. L. *J. Electrochem. Soc.* **1992**, *139*, 654−662.

(13) Po, H. N. *Coord. Chem. Rev.* **1976**, *20*, 171−195.

(14) Mentasti, E.; Baiocchi, C.; Coe, J. S. *Coord. Chem. Rev.* **1984**, *54*, 131−157.

(15) Bushnell, G. W.; Kahn, M. A. *Can. J. Chem.* **1972**, *50*, 315−323.

(16) (a) Collins, D. M.; Scheidt, W. R.; Hoard, J. L. *J. Am. Chem. Soc.* **1972**, *94*, 6689−6696. (b) Scheidt, W. R.; Mondal, J. U.; Eigenbrot, C. W.; Adler, A.; Radonovich, L. J.; Hoard, J. L. *Inorg. Chem.* **1986**, *25*, 795−799. (c) Wong, W-K.; Zhang, L.; Wong, W-T.; Xue, F.; Mak, T. C. W. *J. Chem. Soc., Dalton Trans.* **1999**, 615−622. (d) Ishii, T.; Aizawa, N.; Kanehama, R.; Yamashita, M.; Matsuzaka, H.; Kodama, T.; Kikuchi, K.; Ikemoto, I. *Inorg. Chim. Acta* **2001**, *317*, 81−90. (e) Dorough, G. D.; Miller, J. R.; Huennekens, F. M. *J. Am. Chem. Soc.* **1951**, *73*, 4315−4320. (f) Aizawa, N.; Hara, H.; Ishii, T.; Yamashita, M.; Miyasaka, H.; Matsuzaka, H.; Kodama, T.; Kikuchi, K.; Ikemoto, I. *Mol. Cryst. Liq. Cryst. Sect. A* **2002**, *376*, 13−18. (g) Senge, M. O.; Runge, S.; Speck, M.; Ruhlandt-Senge, K. *Tetrahedron* **2000**, *56*, 8927−8932.

(17) (a) Mertes, K. B. *Inorg. Chem.* **1978**, *17*, 49−52. (b) Po, H. N; Shen, S-C.; Doedens, R. J. *Acta Crystallogr., Sect. C*: *Cryst. Struct. Commun.* **1993**, *49*, 1914−1916. (c) Ito, T.; Ito, H.; Toriumi, K. *Chem. Lett.* **1981**, 1101−1104. (d) Po, H. N.; Brinkman, E.; Doedens, R. J. *Acta Crystallogr., Sect. C*: *Cryst. Struct. Commun.* **1991**, *47*, 2310−2312. (e) Wang, Q-M.; Mak, T. C. W. *Chem Comm.* **2001**, 807−808. (f) Wang, Q-M.; Lee, H. K.; Mak, T. C. W. *New J. Chem.* **2002**, *26*, 513−515.

(18) (a) Atwood, J. L.; Simms, M. L.; Zatko, D. A. *Cryst. Struct. Commun.* **1973**, *2*, 279−281. (b) Drew, M. G. B.; Matthews, R. W.; Walton, R. A. *J. Chem. Soc. A* **1970**, 1405−1410. (c) Drew, M. G. B.; Matthews, R. W.; Walton, R. A. *J. Chem. Soc. A* **1971**, 2959−2962.

(19) (a) Levason, W.; Spicer, M. D. *Coord. Chem. Rev.* **1987**, *76*, 45−120. (b) McMillan, J. A. *Chem. Rev.* **1962**, *62*, 65−80. (c) McMillan, J. A.; Smaller, B. *J. Chem. Phys.* **1961**, *35*, 1698−1701. (d) Leung, P. C.; Aubke, F. *Inorg. Chem.* **1978**, *17*, 1765−1772.

(20) Evans, J. C.; Gillard, R. D.; Lancashire, R. J.; Morgan, P. H. *J. Chem. Soc. Dalton Trans.* **1980**, 1277−1281.

(21) (a) Halpern, T.; McKoskey, S. M.; McMillan, J. A. *J. Chem. Phys.* **1970**, *52*, 3526−3529. (b) Halpern, T.; Phillips, D. W.; McMillan, J. A. *J. Chem. Phys.* **1970**, *52*, 5548−5550.

(22) Williams, R.; Billig, E.; Waters, J. H.; Gray, H. B. *J. Am. Chem. Soc.* **1966**, *88*, 43−50.

(23) Kundu, T. K.; Manoharan, P. T. *Mol. Phys.* **2000**, *98*, 2007−2019.

(24) Kirmse, R.; Windsch, W.; Hoyer, E. *Z. Anorg. Allg. Chem.* **1971**, *386*, 213−220.

(25) Ansell, C. W. G.; Lewis, J.; Liptrot, M. C.; Raithby, P. R.; Schröder, M. *J. Chem. Soc. Dalton Trans.* **1982**, 1593−1601.

(26) Blake, A. J.; Gould, R. O.; Holder, A. J.; Hyde, T. I.; Schröder, M. *J. Chem. Soc. Dalton Trans.* **1988**, 1861−1865.

(27) (a) Ansell, C. W. G.; Lewis, J.; Raithby, P. R.; Ramsden, J. N.; Schröder, M. *J. Chem. Soc. Chem. Commun.* **1982**, 546−547. (b) Lewis, J.; Schröder, M. *J. Chem. Soc. Dalton Trans.* **1982**, 1085−1089. (c) Wang, Q.; Barclay, E.; Blake, A. J.; Davies, E. S.; Evans, D. J.; Marr, A. C.; McInnes, E. J. L.; McMaster, J.; Wilson, C.; Schröder, M. *Chem.−Eur. J.* **2004**, *10*, 3384−3396.

(28) (a) Blake, A. J.; Gould, R. O.; Halcrow, M. A.; Holder, A. J.; Hyde, T. I.; Schröder, M. *J. Chem. Soc. Dalton Trans.* **1992**, 3427−3431. (b) Branscombe, N. D. M. J.; Atkins, A. J.; Marin-Becerra, A.; McInnes, E. J. L.; Mabbs, F. E.; McMaster, J.; Schröder, M. *Chem. Comm.* **2003**, 1098−1099.

(29) (a) Blake, A. J.; Gould, R. O.; Hyde, T. I.; Schröder, M. *J. Chem. Soc. Chem. Commun.* **1987**, 431−433. (b) Reid, G.; Blake, A. J.; Hyde, T. I.; Schröder, M. *J. Chem. Soc. Chem. Commun.* **1988**, 1397−1399. (c) Blake, A. J.; Gould, R. O.; Hyde, T. I.; Schröder, M. *J. Chem. Soc. Chem. Commun.* **1987**, 1730−1732.

(30) (a) Blake, A. J.; Holder, A. J.; Hyde, T. I.; Schröder, M. *J. Chem. Soc. Chem. Commun.* **1987**, 987−988. (b) Blake, A. J.; Gordon, L. M.; Holder, A. J.; Hyde, T. I.; Reid, G.; Schröder, M. *J. Chem. Soc. Chem. Commun.* **1988**, 1452−1454. (c) Blake, A. J.; Reid, G.; Schröder, M. *J. Chem. Soc. Dalton Trans.* **1990**, 3363−3373.

(31) Brown, A. R.; Guo, Z.; Mosselmans, J. F. W.; Parsons, S.; Schröder, M.; Yellowlees, L. J. *J. Am. Chem. Soc.* **1998**, *120*, 8805−8811.

(32) Blake, A. J.; Gould, R. O.; Holder, A. J.; Hyde, T. I.; Lavery, A. J.; Odulate, M. O.; Schröder, M. *J. Chem. Soc. Chem. Commun.* **1987**, 118−120.

(33) (a) Blake, A. J.; Schröder, M. *Adv. Inorg. Chem.* **1990**, *35*, 1−81. (b) Reid, G.; Schröder, M. *Chem. Soc. Rev.* **1990**, *19*, 239−269. (c) Schröder, M. *Pure App. Chem.* **1988**, *60*, 517−524. See also: (d) Gould, R. O.; Lavery, A. J.; Schröder, M. *J. Chem. Soc. Chem. Commun.* **1985**, 1492−1493. (e) Blake, A. J.; Holder, A. J.; Hyde, T. I.; Küppers, H.-J.; Schröder, M.; Stötzel, S.; Wieghardt, K. *J. Chem. Soc. Chem. Commun.* **1989**, 1600−1602.
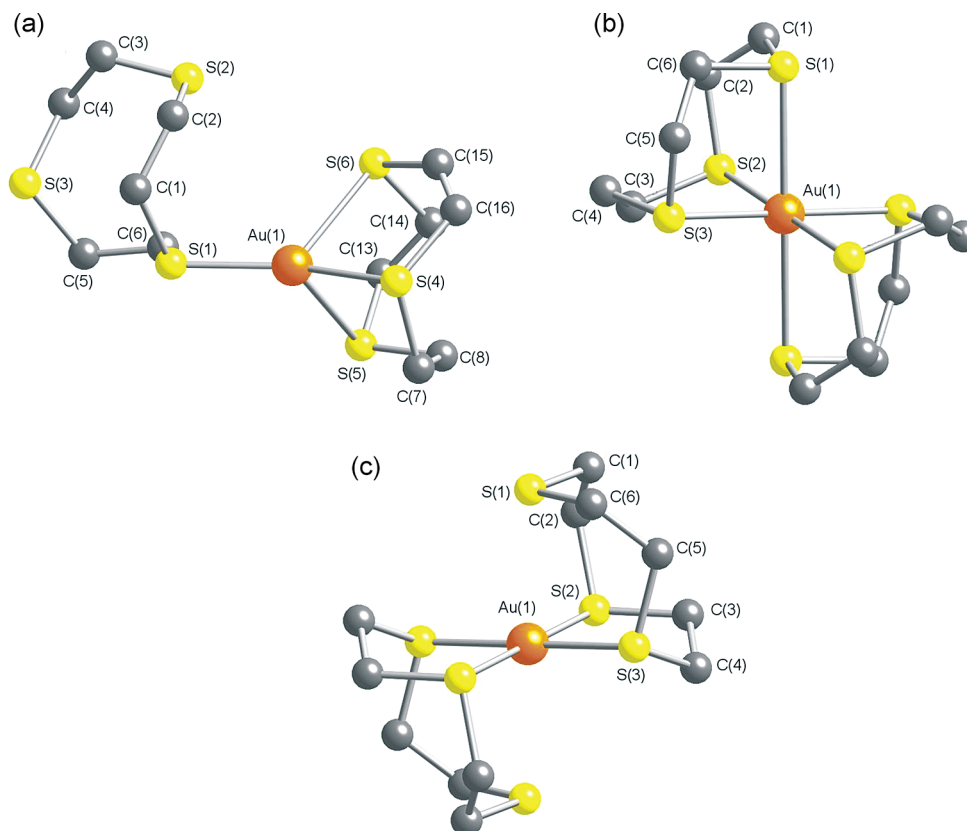
**Figure 1.** Views of single-crystal X-ray structures of (a) [Au([9]aneS$_3$)$_2$]$^+$, (b) [Au([9]aneS$_3$)$_2$]$^{2+}$, and (c) [Au([9]aneS$_3$)$_2$]$^{3+}$.[34,35a]

complexes with thioether crowns have been the subject of other reports. The structural characterization of Ag(II) with thioether donor ligands has not been reported previously, and this is the first comprehensive and detailed study by multifrequency EPR spectroscopy, with simulations of high quality data linked to DFT calculations to probe the degree of redox non-innocence of thioether crowns in these complexes.

The thioether macrocycles [9]aneS$_3$ (1,4,7-trithiacyclononane) and [18]aneS$_6$ (1,4,7,10,13,16-hexathiacyclooctadecane) (see Chart 1) are well-known to be capable of modifying their coordination to accommodate a range of transition-metal stereochemistries and, as such, are suited to facilitate the study of the redox chemistry of transition metal complexes.[33] [9]aneS$_3$

**Chart 1.** [9]aneS$_3$ (i) and [18]aneS$_6$ (ii)
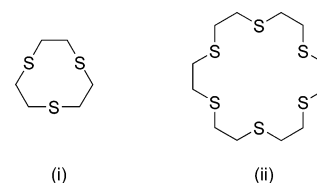


typically favors facial coordination and forms sandwich-type complexes,[33] whereas [18]aneS$_6$ is large enough to encapsulate a metal ion.[40]

## Results and Discussion

**Synthesis and Characterization of [Au([9]aneS$_3$)$_2$](BF$_4$)$_2$.** The binding of Au(I), Au(II), and Au(III) centers in the complexes [Au([9]aneS$_3$)$_2$]$^{+/2+/3+}$ and their single-crystal X-ray structures have been reported (Figure 1).[34,35] [Au([9]aneS$_3$)$_2$]-(BF$_4$)$_2$ was prepared by reaction of 2 equiv of [9]aneS$_3$ under reflux with 1 equiv of HAuCl$_4$ in HBF$_4$ (50%) for 30 min in the absence of light. We sought to determine the degree of delocalisation of charge in [Au([9]aneS$_3$)$_2$]$^{2+}$ and to probe the degree of non-innocence of the thioether donors in this system.

**Multi-Frequency EPR Studies on [Au([9]aneS$_3$)$_2$]$^{2+}$.** [Au([9]aneS$_3$)$_2$]$^{2+}$ was studied in MeCN/toluene solution (*ca.* 10:1 v/v) as a fluid and as a frozen solution by multifrequency L-, S-, X-, K- and Q-band EPR spectroscopy. The fluid solution

(34) Blake, A. J.; Greig, J. A.; Holder, A. J.; Hyde, T. I.; Taylor, A.; Schröder, M. *Angew. Chem., Int. Ed. Engl.* **1990**, *29*, 197−198.

(35) (a) Blake, A. J.; Gould, R. O.; Greig, J. A.; Holder, A. J.; Hyde, T. I.; Schröder, M. *J. Chem. Soc. Chem. Commun.* **1989**, 876−878. (b) Blake, A. J.; Taylor, A.; Schröder, M. *J. Chem. Soc. Chem. Commun.* **1993**, 1097−1098.

(36) (a) Ihlo, L.; Kampf, M.; Böttcher, R.;. Kirmse, R. *Z. Naturforsch.* **2002**, *57b*, 171−176. (b) Kampf, M.; Olk, R.-M.; Kirmse, R. *Z. Anorg. Allg. Chem.* **2002**, *628*, 34−36.

(37) Kampf, M; Griebel, J; Kirmse, R. *Z. Anorg. Allg. Chem.* **2004**, *630*, 2669−2676.

(38) (a) Blower, P. J.; Clarkson, J. A.; Rawle, S. C. Hartman, J. R.; Wolf, R. E.; Yagbasan, R.; Bott, S. G.; Cooper, S. R. *Inorg. Chem.* **1989**, *28*, 4040−4046. (b) Clarkson, J.; Yagbasan, R.; Blower, P. J.; Rawle, S. C.; Cooper, S. R. *J. Chem. Soc. Chem. Comm.* **1987**, 950−951. (c) Blake, A. J.; Collison, D.; Gould, R. O.; Reid, G.; Schröder, M. *J. Chem. Soc. Dalton Trans.* **1993**, 521−531. (d) Blake, A. J.; Gould, R. O.; Reid, G.; Schröder, M. *J. Chem. Soc. Commun.* **1990**, 974−976. (e) Blake, A. J.; Gould, R. O.; Holder, A. J.; Hyde, T. I.; Reid, G.; Taylor, A.; Schröder, M.; Collison, D. In *NATO Advanced Workshop on Molecular Electrochemistry of Inorganic, Bioinorganic and Organometallic Compounds*; Pombeiro, A. J. L., McCleverty, J. A., Eds.; NATO Meeting/NATO ASI Series, Vol. 385; Kluwer Academic Publishers: Norwell, MA, 1993; 121−129.

(39) (a) Blake, A. J.; Gould, R. O.; Holder, A. J.; Hyde, T. I.; Schröder, M. *Polyhedron* **1989**, *8*, 513−518. (b) Blake, A. J.; Gould, R. O.; Parsons, S.; Radek, C.; Schröder, M. *Angew. Chem., Int. Ed. Engl.* **1995**, *34*, 2374−2376.

(40) (a) Hintsa, E. J.; Hartman, J. R.; Cooper, S. R. *J. Am. Chem. Soc.* **1983**, *105*, 3738−3739. (b) Hartman, J. R.; Cooper, S. R. *J. Am. Chem. Soc.* **1986**, *108*, 1202−1208. (c) Hartman, J. R.; Hintsa, E. J.; Cooper, S. R. *J. Am. Chem. Soc.* **1986**, *108*, 1208−1214. (d) Blake, A. J.; Gould, R. O.; Lavery, A. J.; Schröder, M. *Angew. Chem., Int. Ed. Engl.* **1986**, *25*, 274−276.
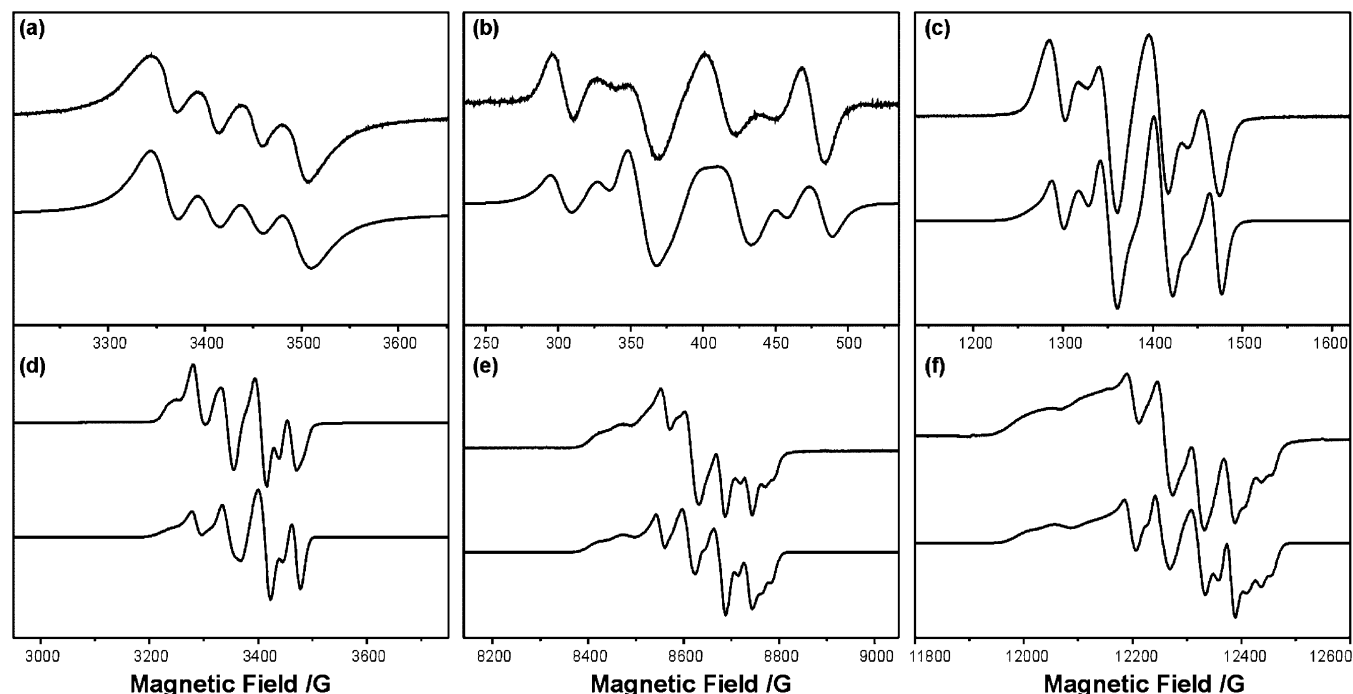
**Figure 2.** EPR spectra of [Au([9]aneS$_3$)$_2$]$^{2+}$ in MeCN/toluene solution: (a) X-band fluid spectrum at room temperature (top) and simulation (below) with $g_{iso} = 2.005$, $A_{iso(Au)} = -43 \times 10^{-4}$ cm$^{-1}$, with Gaussian linewidths of $W_{iso} = 40$ G (bottom). (b) L-band, (c) S-band, (d) X-band, (e) K-band, and (f) Q-band spectra at *ca.* 110 K (top) and simulation (below) with $g_{xx} = 1.999$, $g_{yy} = 1.980$, $g_{zz} = 2.032$, $A_{xx(Au)} = -50 \times 10^{-4}$ cm$^{-1}$, $A_{yy(Au)} = -30 \times 10^{-4}$ cm$^{-1}$, $A_{zz(Au)} = -50 \times 10^{-4}$ cm$^{-1}$, $P = \eta = 5 \times 10^{-4}$ cm$^{-1}$, and a twist about the *x*-axis of the quadrupole tensor with respect to the *g* and *A* matrices by $\rho = 15°$.

X-band spectrum at room temperature (Figure 2a) comprises four evenly spaced transitions due to the hyperfine interaction with the $^{197}$Au nucleus ($I = 3/2$, 100% natural abundance). Simulation gives $g_{iso} = 2.005$, $A_{iso} = -43 \times 10^{-4}$ cm$^{-1}$ (the sign of $A_{iso}$ will be justified later). On freezing this solution at *ca.* 110 K, the X-band spectrum is dominated by a $^{197}$Au hyperfine quartet (Figure 2d), which indicates that the *g* anisotropy is not very large. At Q-band, there is a partial resolution of all three *g* values, confirming the rhombic nature of the *g* matrix, with hyperfine quartets centered at $g_{xx} = 1.999$, $g_{yy} = 1.980$, $g_{zz} = 2.032$ (Figure 2f). From simple crystal field arguments on this Jahn−Teller elongated, nominally Au(II), 5d$^9$ complex, we expect the SOMO to be a formal d$_{xy}$ orbital where the *xy* plane is defined by the equatorial AuS$_4$ plane, and we would expect the largest *g* value ($g_{zz}$) to be normal to this plane. At Q-band, the central $^{197}$Au hyperfine quartet (to $g_{xx}$) is clearly resolved at $|A_{xx}| \approx 50$ G, as are the three highest field lines of the quartet to $g_{yy}$ (the lowest field transition of $g_{yy}$ overlaps with the highest field transition of $g_{xx}$); $|A_{yy}|$ is considerably smaller, at *ca.* 30 G. All four transitions of the lowest field, $g_{zz}$ hyperfine quartet are resolved, although with the larger experimental linewidths at Q-band (*cf.* X-band), they appear as two sets of two partially resolved peaks. At the intermediate K-band frequency, the separation of the two lowest-field peaks is observed more clearly at the cost of a lower resolution of the *g* anisotropy. From the separations, $|A_{zz}|$ is of a similar magnitude to $|A_{xx}|$. At microwave frequencies lower than K-band, the poor resolution of the *g* anisotropy is such that the frozen solution spectra appear near-axial due to the near-axial pattern of $^{197}$Au hyperfine couplings.

The four transitions of the central hyperfine quartet, to $g_{xx}$, are more-or-less evenly spaced, as is apparent from every frequency measured. In contrast, a closer inspection of the K-

and Q-band spectra (Figure 2e,f) reveals that the lowest and highest field quartets ($g_{zz}$ and $g_{yy}$, respectively) are *unevenly* spaced, being grouped into "two-plus-two" peaks, i.e., the separation between the inner two transitions is greater than those between the outer and inner transitions. This is indicative of large quadrupole coupling to the $I = 3/2$ $^{197}$Au nucleus (which has a very large nuclear quadrupole moment) of similar magnitude to the nuclear hyperfine interaction.

**Simulations.** The spectra were simulated using the spin-Hamiltonian:

$$\hat{H} = \beta_e \mathbf{g}B\hat{S} + \hat{S}\mathbf{A}\hat{I} + g_n\beta_n B\hat{I} + P_{zz}[3\hat{I}_z^2 - I(I+1)] + (P_{xx} - P_{yy})(\hat{I}_x^2 - \hat{I}_y^2)$$

where $\beta_e$ and $\beta_n$ are the electronic and $^{197}$Au nuclear Bohr magnetons, respectively, $B$ is the applied magnetic field, $g$ and $A$ are the electronic *g* matrix and $^{197}$Au nuclear hyperfine matrix, respectively, and $P_{ii}$ ($i = x, y, z$) are the principal values of the nuclear quadrupole interaction tensor $P$, defined by:

$$P_{ii} = \frac{eQq_{ii}}{2I(2I-1)}$$

and

$$q_{ii} = \frac{\partial^2 V}{\partial i^2}$$

where $e$ is the electronic charge, $Q$ is the quadrupole moment of the $^{197}$Au nucleus and $q_{ii}$ are the principal values of the electric field gradient at the nucleus. The $P$ tensor is traceless; thus, its principal components can be parametrized by $P = [P_{zz} - (P_{xx} + P_{yy})/2]/3$ and a rhombic term $\eta = (P_{xx} - P_{yy})/2$.
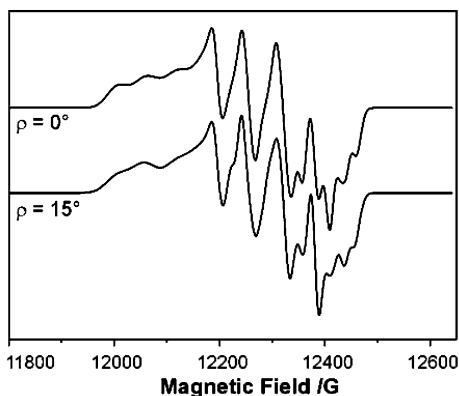
**Figure 3.** Effect of the angle of non-co-incidence $\rho$ between the $g$, $A$ hyperfine matrices and the quadrupole tensor $P$ on the simulated Q-band spectra (34.280 GHz) of $[Au([9]aneS_3)_2]^{2+}$. Simulation parameters: $g_{xx} = 1.999$, $g_{yy} = 1.980$, $g_{zz} = 2.032$, $A_{xx(Au)} = -50 \times 10^{-4}$ cm$^{-1}$, $A_{yy(Au)} = -30 \times 10^{-4}$ cm$^{-1}$, $A_{zz(Au)} = -50 \times 10^{-4}$ cm$^{-1}$, $P = \eta = 5 \times 10^{-4}$ cm$^{-1}$. Angle of rotation about the $x$-axis $\rho = 0$ (top) and 15° (bottom). Gaussian linewidths of $W_{xx} = W_{yy} = 8$ G, $W_{zz} = 22$ G.



**Figure 4.** Effect of the Au quadrupole tensor rhombicity parameter $\eta$ on the simulated Q-band spectra (34.280 GHz) of $[Au([9]aneS_3)_2]^{2+}$. Simulation parameters: $g_{xx} = 1.999$, $g_{yy} = 1.980$, $g_{zz} = 2.032$, $A_{xx(Au)} = -50 \times 10^{-4}$ cm$^{-1}$, $A_{yy(Au)} = -30 \times 10^{-4}$ cm$^{-1}$, $A_{zz(Au)} = -50 \times 10^{-4}$ cm$^{-1}$, $P = 5 \times 10^{-4}$ cm$^{-1}$, $\rho = 15°$, with $\eta = 0$ (top) and $5 \times 10^{-4}$ cm$^{-1}$ (bottom). Gaussian linewidths of $W_{xx} = W_{yy} = 8$ G, $W_{zz} = 22$ G.
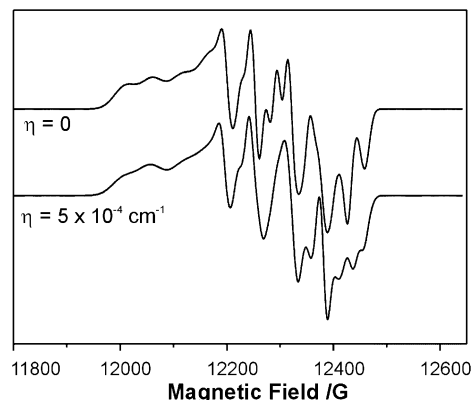
We initially simulated the spectra by ignoring the quadrupole interaction to define the electronic $g$ values and to obtain best first estimates of the principal values for the hyperfines. These simulations were performed first at the higher frequencies (K-, Q-band) and then the values checked by simulation of the lower frequency spectra. It was assumed that the principal axes of the $g$ and $A$ matrices were co-incident. This approach defines $g_{xx}$, $g_{yy}$, $g_{zz}$, and $A_{xx}$ well, but poorly defines $A_{yy}$ and $A_{zz}$ due to the large influence of the quadrupole coupling on these multiplets. We then introduced a non-zero value of the quadrupole parameter $P$ (Figures 3 and 4). For values of $P > ca. 5 \times 10^{-4}$ cm$^{-1}$, new transitions are found in the calculated spectra beyond the high-field edge of the spectrum calculated for $P = 0$ (and the experimental spectrum). This places an upper limit of $5 \times 10^{-4}$ cm$^{-1}$ on our value of $P$. The $P$ tensor elements ($/10^{-4}$ cm$^{-1}$) for $P = 5 \times 10^{-4}$ cm$^{-1}$, $\eta = 0$ would be:

$$\begin{pmatrix} -5 & 0 & 0 \\ 0 & -5 & 0 \\ 0 & 0 & +10 \end{pmatrix}$$

The most significant changes to the calculated spectra (*cf.* $P = 0$) were found to be in the $x$ and $y$ (middle- and high-field) features. However, experimentally we know that $x$ is largely unaffected by quadrupole effects (because $g_{xx}$ is split as a regular four line multiplet) whereas $y$ and $z$ are affected as revealed by the uneven spacings in the quartets. Therefore, we introduced a non-zero value for the rhombic quadrupole parameter $\eta$. When $\eta = P$, there is a special case in which $P_{xx} = 0$; the $P$ tensor elements ($/10^{-4}$ cm$^{-1}$) for $P = \eta = 5 \times 10^{-4}$ cm$^{-1}$ become:

$$\begin{pmatrix} 0 & 0 & 0 \\ 0 & -10 & 0 \\ 0 & 0 & +10 \end{pmatrix}$$

Thus, $\eta = P$ restricts the quadrupole effects to the $yz$ plane. The inclusion of $P = \eta = 5 \times 10^{-4}$ cm$^{-1}$ does not perturb the central $g_{xx}$ multiplet in the calculated spectrum. However, there is a slight modulation of the relative spacing and intensities of the four transitions within the $g_{zz}$ (low-field) and $g_{yy}$ (high-field) quartets (Figure 4). These effects are quite subtle and not large enough to reproduce the distinct "two-plus-two" patterns

observed experimentally. However, we found that these uneven spacings in $y$ and $z$ can be enhanced by including an angle of non-co-incidence between the $P$ tensor axes with those of the $g$ and $A$ matrices which are assumed to have co-incident principal axes. We explored the effect of a single angle of rotation of the $P$ tensor about the $x$-axis. This has the effect of mixing the $y$ and $z$ components, introducing non-zero off-diagonal $P_{yz}$ and $P_{zy}$ elements. We rotate about $x$ because in the experimental spectra we observe that the $g_{xx}$ hyperfine multiplet is not affected by quadrupole coupling, and rotation about $y$ or $z$ would reintroduce quadrupole effects to $g_{xx}$. Thus, the $x$-axis of the $P$ tensor is co-incident with those of the $g/A$ matrices, but the $y$ and $z$ axes are rotated through an angle $\rho$ about the $x$-axis. The effect of $\rho$ for fixed $P = \eta$ is shown in Figure 3, and the large effect on the uneven spacing of the $g_{yy}$ and $g_{zz}$ features can be clearly seen. We found the best fit to the experiment with $\rho = 15°$ for $P = \eta = 5 \times 10^{-4}$ cm$^{-1}$; this gives the $P$ tensor elements ($/10^{-4}$ cm$^{-1}$) in the diagonal $g/A$ frame:

$$\begin{pmatrix} 0 & 0 & 0 \\ 0 & -8.7 & -5.0 \\ 0 & -5.0 & +8.7 \end{pmatrix}$$

Thus, there are no quadrupole effects on the $x$ features of the calculated spectra, and significant off-diagonal $yz$ elements produce the pronounced "two-plus-two" structure in both the $y$ and $z$ components. Note that it is not possible to simulate the spectra by including non-co-incidence effects with $\eta = 0$, for example see Figure 4, as this still gives rise to a significant $P_{xx}$ component. Thus, to reproduce the experimentally observed "two-plus-two" distortions of the $g_{yy}$ and $g_{zz}$ hyperfine multiplets, it is necessary to include non-zero values for *both* these parameters. Figures 3 and 4 also highlight the sensitivity of the calculated spectra to changes in $\eta$ and $\rho$; hence, these parameters can be determined with some confidence.

To establish a best set of parameters, we varied $A_{yy}$, $A_{zz}$, $P$, $\eta$, and $\rho$ to simulate the Q-band spectrum with the set of $A_{xx}$, $g_{xx}$, $g_{yy}$, and $g_{zz}$ parameters established previously. All the parameters were then refined by simulating the lower frequency spectra, which are more sensitive to changes in $A_{ii}$, and the process repeated iteratively until excellent simulations were

achieved for **all** frequencies studied with a single set of parameters ignoring minor changes in linewidths. The final parameters were: $g_{xx} = 1.999$, $g_{yy} = 1.980$, $g_{zz} = 2.032$, $A_{xx} = -50 \times 10^{-4}$ cm$^{-1}$, $A_{yy} = -30 \times 10^{-4}$ cm$^{-1}$, $A_{zz} = -50 \times 10^{-4}$ cm$^{-1}$, $P = 5 \times 10^{-4}$ cm$^{-1}$, $\eta = 5 \times 10^{-4}$ cm$^{-1}$, and $\rho = 15°$. The assignment of the signs of $A_{ii}$ will be justified below.

**Interpretation of EPR Data for [Au([9]aneS$_3$)$_2$]$^{2+}$.** EPR spectra have been reported for Au(II)-doped [Zn([9]aneS$_3$)$_2$]-(BF$_4$)$_2$ by Kirmse et al.[36] However, the spectra obtained are of significantly lower resolution than in the present study, in particular at the higher frequencies and are found to be temperature dependent, which presumably reflects structural changes in the host Zn(II) lattice. The authors present simulations only for S- and W-band, based on the parameters $g_1 = 2.004$, $g_2 = 1.989$, $g_3 = 2.041$, $A_1 = -55 \times 10^{-4}$ cm$^{-1}$, $A_2 = -35 \times 10^{-4}$ cm$^{-1}$, $A_3 = -43 \times 10^{-4}$ cm$^{-1}$, $P_1 = +10 \times 10^{-4}$ cm$^{-1}$, $P_2 = -7 \times 10^{-4}$ cm$^{-1}$, $P_3 = -3 \times 10^{-4}$ cm$^{-1}$ (equivalent to $P = 5 \times 10^{-4}$ cm$^{-1}$, $\eta = 2 \times 10^{-4}$ cm$^{-1}$) where the $g$ and $A$ matrices and the $P$ tensor are all assumed to have co-incident principal axes. However, these fail to reproduce the "two-plus-two" patterns of the hyperfine quartets in the high- and low-field features. Our simulations for the frozen and fluid solutions of [Au([9]aneS$_3$)$_2$]$^{2+}$, based on much higher resolution data, give excellent simulations at *all* frequencies giving greater confidence in the parameters, and these are significantly different from those reported by Kirmse.[36a]

To interpret the spectra, we assign $g_{xx}$ and $g_{yy}$ to orientations lying in the equatorial AuS$_4$ plane, with $g_{zz}$ (the largest $g$ value) perpendicular to this plane as would be expected from simple crystal field arguments, with the unpaired electron in the metal 5d$_{xy}$ orbital. DFT calculations are consistent with this interpretation, predicting that the SOMO has a$_g$ symmetry in $C_i$ point symmetry, and that the dominant metal component of the SOMO is 5d$_{xy}$ (see below). In this case, the principal components of the $g$ and $A$ matrices are given by eqs 1 and 2, respectively:[41]

$$g_{xx} = g_e + 2\delta_{xz}$$
$$g_{yy} = g_e + 2\delta_{yz}$$
$$g_{zz} = g_e + 8\delta_{x^2-y^2} \tag{1}$$

and

$$A_{xx} = A_S + P_d\left[\frac{2}{7}a^2 + \Delta g_{xx} - \frac{3}{14}\Delta g_{yy}\right]$$
$$A_{yy} = A_S + P_d\left[\frac{2}{7}a^2 + \Delta g_{yy} - \frac{3}{14}\Delta g_{xx}\right]$$
$$A_{zz} = A_S + P_d\left[-\frac{4}{7}a^2 + \Delta g_{zz} + \frac{3}{14}(\Delta g_{xx} + \Delta g_{yy})\right] \tag{2}$$

where $g_e$ is the free-electron $g$ value, $\Delta g_{ii}$ are the shifts of the $g$ values from $g_e$, $P_d$ is the electron-nuclear dipolar coupling parameter for Au 5d electrons, and $a$ is the linear combination of atomic orbitals (LCAO) coefficient of the Au 5d$_{xy}$ orbital in the SOMO. The $\delta_i$ terms are the weighted average ground state-excited-state energy gaps:

$$\delta_i = \sum_{k \neq 0} \frac{\lambda c_{ik}^2}{E_0 - E_k}$$

where $\lambda$ is the spin–orbit coupling constant for Au 5d electrons, and $c_{ik}$ is the LCAO coefficient of the $i$th atomic orbital in the $k$th molecular orbital. $A_S$ is the isotropic Fermi contact term given by:

$$A_S = \langle A \rangle - P_d\left(\frac{\Delta g_{xx} + \Delta g_{yy} + \Delta g_{zz}}{3}\right) \tag{3}$$

and can include contributions from direct admixture of 6s orbital density to the SOMO and from inner core polarization.

From eqs 1 we expect $g_{zz}$ to be the largest $g$ value, oriented perpendicular to the plane of the formal 5d$_{xy}$ orbital, and this is the basis of our assignment of $z$ (see above). $g_{xx}$ and $g_{yy}$ are both less than $g_e$, which is not expected from eq 1. One possible explanation for this is that eq 1 arises from a first-order perturbation treatment of the spin–orbit coupling, and this has been noted to be inadequate in some heavy metal complexes where second-order terms in $\lambda^2$ can be significant.[41] Significant negative contributions to the $g$-shifts can also arise from low-energy charge-transfer transitions from or to predominantly ligand-based orbitals, and this has been observed to give rise to negative $g$ shifts in several {Au(II)S$_4$} complexes.[1,2,6b,7b,7c,37,42]

The principal values of the $A$ matrix, determined by simulation, average to the experimentally measured isotropic value ($\langle A \rangle = A_{iso} = 43 \times 10^{-4}$ cm$^{-1}$), and hence, all $A_{ii}$ values must be the same sign as each other and as $A_{iso}$. With this information, eq 2 implies that $|A_{zz}|$ should be the largest principal value of the $A$ matrix. Although we find $A_{zz}$ to be larger than $A_{yy}$, it is of similar magnitude to $A_{xx}$. This may be a limitation of the model used to simulate the spectra; we have assumed that the principal axis of the $g$ and $A$ matrices are co-incident because we achieve good simulations without including this effect. However, this situation is not required for $C_i$ molecular point symmetry, where all the 5d orbitals transform as a$_g$ and hence can mix. This scrambling of d-orbital functions can give rise to $g/A$ matrix non-co-incidence effects.[43] DFT calculations (see below) suggest that the dominant contribution to the SOMO is 5d$_{xy}$ (27.7%) and that there are negligible contributions from the other 5d orbitals of a$_g$ symmetry. Thus, any rotation about the $g_{yy}/A_{yy}$ axis is likely to be minor. A rotation could have the effect on the frozen solution spectrum of diminishing the separations within the $g_{zz}$ hyperfine quartet while increasing those of $g_{xx}$. We have attempted to include this angle of twist while keeping the sum of $A_{xx}$ and $A_{zz}$ to be close to $-100 \times 10^{-4}$ cm$^{-1}$ and fixing all other parameters to the values above. Although we can achieve reasonable multifrequency simulations in this model, they are not as good as those in Figure 2, and we do not feel that their inclusion here is justified. However, a non-zero twist about $g_{yy}/A_{yy}$ cannot be excluded, and consequently in the analysis of the dipolar part of the metal hyperfine, the contribution of the metal d-orbitals to the SOMO (see below) should be regarded as a minimum value.

(41) (a) Maki, A. H.; Edelstein, N.; Davison, A.; Holm, R. H. *J. Am. Chem. Soc.* **1964**, *86*, 4580−4587. (b) Rieger, P. H. *Coord. Chem. Rev.* **1994**, *135−136*, 203−286.

(42) van Rens, J. G. M.; de Boer, E. *Mol. Phys.* **1970**, *19*, 745−747.
(43) See for example: (a) Carpenter, G. B.; Clark, G. S.; Rieger, A. L.; Rieger, P. H.; Sweigart, D. A. *J. Chem. Soc. Dalton Trans.* **1994**, 2903−2910. (b) Wang, Q.; Barclay, E.; Blake, A. J.; Davies, E. S.; Evans. D. J.; Marr, A. C.; McInnes, E. J. L.; McMaster, J.; Wilson, C.; Schröder, M. *Chem. Eur. J.* **2004**, *10*, 3384−3396.

Combination of eqs 1–3 gives:

$$A_{zz} - \langle A \rangle = P_{d}\left[ -\frac{4}{7}a^2 + \frac{2}{3}\Delta g_{zz} - (\Delta g_{xx} + \Delta g_{zz})/3 \right] \quad (4)$$

From eq 4 and the assignment above, we can calculate $a^2$, the admixture of $5d_{xy}$ to the SOMO, without the need to explicitly assign $x$ and $y$. The calculated $P_d$ values for the metal ion, using Rieger's methodology in which the result is dependent on the configuration assumed,[44] are $+51.8 \times 10^{-4}$, $+48.4 \times 10^{-4}$, and $+51.1 \times 10^{-4}$ cm$^{-1}$ for the possible electronic configurations $5d^8$, $5d^9$, and $5d^86s^1$, respectively. Substitution into eq 4 with the experimental $g$ and $A$ values (assuming negative values of $A_{ii}$) gives $a^2 = 0.29$, 0.30 and 0.29, respectively. [Note that 6p admixture to the $a_g$ SOMO is symmetry forbidden; hence, we neglect the $5d^86p^1$ configuration.] Positive values of $A_{ii}$ give negative values of $a^2$. Thus, the metal d-orbital contribution to the SOMO is *ca.* 30%, although allowing for mixing with $d_{yz}$ may increase this value slightly (see above).

The $C_i$ point symmetry of $[Au([9]aneS_3)_2]^{2+}$ also allows direct admixture of the Au 6s orbital into the $a_g$ SOMO, and this could give rise to the relatively large isotropic component of the $A$ matrix. This can be estimated directly from the ratio of the experimental isotropic hyperfine $A_{iso}$, and the calculated hyperfine coupling for unit population of the 6s orbital in the $5d^86s^1$ configuration, $A_{6s} = 1874 \times 10^{-4}$ cm$^{-1}$ [44] to give 0.02 (2%), although this should be viewed as an upper limit because spin polarization of inner core s electrons can also contribute to the observed isotropic hyperfine. It should be noted that the spin–orbit coupling contribution to $A_{iso}$, the second term in eq 3, is negligible due to the near-zero average $\Delta g$.

**Quadrupole Effects.** Nuclear quadrupole coupling arises from an anisotropic electron density distribution and the resulting electric field gradients (EFGs) at the nucleus. The effect of the quadrupole coupling on an EPR spectrum is crucially dependent on the relative magnitudes of the quadrupole with respect to the hyperfine interaction. When the quadrupole moment of the nucleus is small, and consequently the $|P_{ii}|$ values are small, the intensities and positions of the allowed $\Delta m_I = 0$ hyperfine lines are unaffected, but otherwise forbidden $\Delta m_I > 0$ transitions can become allowed. This is often the case with, for example, Cu(II) and has been studied extensively by Belford and co-workers,[45] among others. When the quadrupole and hyperfine interactions are of similar magnitude, a further effect can be to perturb the otherwise regular spacing and intensities of the $\Delta m_I = 0$ hyperfine transitions, and this has been much less studied. It is this latter effect that we observe in $[Au([9]-aneS_3)_2]^{2+}$. A thorough investigation of these effects on powder EPR spectra has been reported for a range of Ir(II) complexes.[46] Analyses of quadrupole interactions from single-orientation spectra on Au-doped Ni(II) dithiolene species have also been reported.[1,2,7b,7c,42] Through simulation of the EPR spectra of $[Au([9]aneS_3)_2]^{2+}$, we find that the "two-plus-two" distortions of the $g_{zz}$ and $g_{yy}$ hyperfine quartets can only be reproduced by introduction of both a non-zero rhombic quadrupole parameter $\eta$ and a non-zero angle of twist $\rho$ of the $P$ tensor with respect to the $g$ and $A$ matrices about the $x$ axis. Rieger observed a

similar effect in his Ir(II) study, where the hyperfine quartets due to $^{191,193}$Ir ($I = 3/2$) were grouped into quasi 1:2:1 multiplets and could only be modeled including rhombic asymmetry in $P$ and non-co-incidence between $P$ and $A$.[46] For $[Au([9]aneS_3)_2]^{2+}$, we found the principal values of the diagonal $P$ tensor to be $P_{xx} = 0$, $P_{yy} = -10 \times 10^{-4}$ cm$^{-1}$, and $P_{zz} = +10 \times 10^{-4}$ cm$^{-1}$; when expressed in the diagonal $g$, $A$ frame, the non-zero $P$ tensor elements are: $P_{yy} = -8.7 \times 10^{-4}$ cm$^{-1}$, $P_{zz} = +8.7 \times 10^{-4}$ cm$^{-1}$, and $P_{yz} = P_{zy} = -5 \times 10^{-4}$ cm$^{-1}$.

In a simple crystal field model, a $5d^{10}$ configuration would give an isotropic charge distribution and, therefore, zero quadrupole coupling. The quadrupole coupling that would arise from a single hole in the $5d_{xy}$ orbital can be calculated from:[7b,7c]

$$P_{zz} = \frac{1}{4\pi\epsilon_0}\left[ \frac{e^2 Q}{2I(2I-1)} \right]\frac{4}{7}\langle r^{-3}\rangle_{5d} \quad (5)$$

where $\epsilon_0$ is the permittivity of free space, $e$ is the electronic charge, and $Q$ is the nuclear quadrupole moment of the nucleus ($0.574 \times 10^{-24}$ cm$^2$ for $^{197}$Au). Using a value for $\langle r^{-3}\rangle_{5d}$ of 15.64 a.u., calculated for the $5d^9$ configuration using Rieger's methodology,[44] we obtain $P_{zz} = +67 \times 10^{-4}$ cm$^{-1}$ [$P_{xx}$ and $P_{yy}$ would be half this value and of opposite sign]. This value is slightly larger than those previously calculated by Schlupp and Maki[7c] and by van Rens.[7b] Therefore, we can crudely estimate the $5d_{xy}$ contribution to the SOMO of $[Au([9]aneS_3)_2]^{2+}$ from the ratio of the calculated and experimental values of $P_{zz}$ (expressed in the diagonal $P$ frame), giving $a^2 = 0.15$. Although consistent with a highly delocalised SOMO, this $a^2$ value is significantly lower than that determined from analysis of the metal hyperfines (*ca.* 0.30). However, this quadrupole analysis neglects Sternheimer shielding effects due to polarization of the inner shell electrons by the surrounding non-spherical charge distribution. Thus, the calculated value of $P_{zz}$ is an upper limit, and the quadrupole-derived value of $a^2$ is a lower limit. This analysis also neglects the EFG due to the ligand electrons and nuclei, which tends to be opposite in sign to the metal valence contribution.[43,47] This implies that the valence contribution to $P_{zz}$ is larger than the observed value, and again this would result in a calculated value of $a^2$ that is too low. Belford has used Mulliken population analyses, based on MO calculations, to estimate the metal valence contributions to the EFG.[47] We have followed his methodology using the Mulliken populations derived from DFT calculations using TDZP (Au) and TZP (C, H, S) basis sets. It should be noted that these DFT results are in excellent agreement with the analyses of the metal hyperfine data in terms of the covalency of the SOMO. Table 1 gives the Mulliken populations of the Au 5d orbitals for a free $5d^9$ ion and for $[Au([9]aneS_3)_2]^{2+}$ derived from DFT. The calculated value of $P_{zz}$ for the free ion ($67 \times 10^{-4}$ cm$^{-1}$) is exactly equivalent to that from eq 5. The calculated Mulliken populations for $[Au([9]aneS_3)_2]^{2+}$ give a covalency reduction factor of 0.31, which give $P_{zz} = 21 \times 10^{-4}$ cm$^{-1}$, which is still significantly larger than the experimental value of $10 \times 10^{-4}$ cm$^{-1}$. Thus, to reproduce the experimental metal quadrupole coupling, we require a ligand contribution of *ca.* $-11 \times 10^{-4}$ cm$^{-1}$, which is of the same order of magnitude as found by Belford for square planar $\{Cu(II)S_4\}$ complexes.[47]

(44) Rieger, P. H. *J. Magn. Reson.* **1997**, *124*, 140–146.
(45) Liczwek, D.; Belford, R. L.; Pilbrow, J. R.; Hyde, J. S. *J. Phys. Chem.* **1983**, *87*, 2509–2512 and references therein.
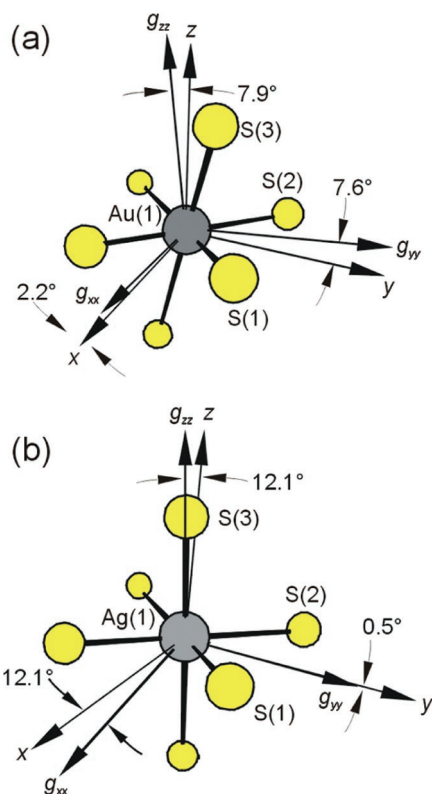(46) Connelly, N. G.; Emslie, D. J. H.; Klangsinsirikul, P.; Rieger, P. H. *J. Phys. Chem. A* **2002**, *106*, 12214–12220.
(47) (a) White, L. K.; Belford, R. L. *Chem. Phys. Lett.* **1976**, *37*, 553–555; (b) White, L. K.; Belford, R. L. *J. Am. Chem. Soc.* **1976**, *98*, 4428–4438.

**Table 1.** 5d Contribution to the EFG from Mulliken Population Analyses

| | $\langle 3\cos^2\theta - 1\rangle$ | free ion population ($n_i$) | $n_i\cdot\langle 3\cos^2\theta - 1\rangle$ | AuS$_6$ population ($n_i$)$^a$ | $n_i\cdot\langle 3\cos^2\theta - 1\rangle$ |
|---|---|---|---|---|---|
| Au 5d$_{x^2-y^2}$ | −4/7 | 2 | −8/7 | 1.97 | −1.13 |
| Au 5d$_{xy}$ | −4/7 | 1 | −4/7 | 1.68 | −0.96 |
| Au 5d$_{xz}$ | 2/7 | 2 | 4/7 | 1.97 | 0.57 |
| Au 5d$_{yz}$ | 2/7 | 2 | 4/7 | 1.97 | 0.57 |
| Au 5d$_{z^2}$ | 4/7 | 2 | 8/7 | 1.98 | 1.13 |
| Sum | | 9 | 0.57$^b$ | 9.57 | 0.18 |
| $\langle r^{-3}\rangle\sum n_i\cdot\langle 3\cos^2\theta - 1\rangle$/a.u. | | | 8.91 | | 2.81 |
| covalency reduction factor | | | 1.00 | | 0.31 |
| $P_{zz}$/10$^{-4}$ cm$^{-1}$ | | | 67 | | 21 |

$^a$ Mulliken populations from DFT calculations using TZ2P basis set. $^b$ Equivalent to the 4/7 term in eq 5.



**Figure 5.** Orientation of the *g* matrices with respect to the Cartesian frame for (a) [Au([9]aneS$_3$)$_2$]$^{2+}$ and (b) [Ag([18]aneS$_6$)]$^{2+}$ calculated with a TZ2P basis set for Au and Ag, respectively, at a TZP basis set for all other atoms.

**Table 2.** Comparison of Spin-Hamiltonian Parameters of [Au([9]aneS$_3$)$_2$]$^{2+}$ with {Au(II)S$_4$} Complexes

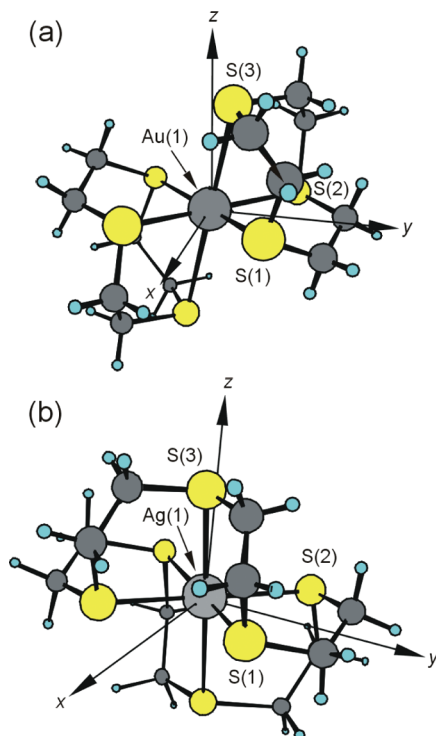| | $g_{xx}$$^a$ | $g_{yy}$$^a$ | $g_{zz}$$^a$ | $A_{xx}$$^b$ | $A_{yy}$ | $A_{zz}$ | $P_{xx}$$^b$ | $P_{yy}$ | $P_{zz}$ |
|---|---|---|---|---|---|---|---|---|---|
| [Au(mnt)$_2$]$^{2-c,f}$ | 2.006 | 1.978 | 2.016 | −41 | −39 | −42 | −7 | −19 | +26 |
| [Au(dmit)$_2$]$^{2-d,f}$ | 2.002 | 1.982 | 2.042 | −40 | −39 | −41 | −6 | −17 | +23 |
| [Au(dtc)$_2$]$^{e,f}$ | 2.008 | 1.986 | 2.118 | −32 | −32 | −30 | −19 | −9 | +28 |
| [Au(9aneS$_3$)$_2$]$^{2+}$ | 1.999 | 1.980 | 2.032 | −50 | −30 | −50 | 0 | −10 | +10 |

$^a$ *z*-axis is perpendicular to AuS$_4$ plane, *y*-axis bisects S−Au−S chelate angles. $^b$ Diagonal elements of $A_{ii}$, $P_{ii}$ in 10$^{-4}$ cm$^{-1}$. $^c$ Data from reference 7c. Note $P_{ii}$ elements have been doubled compared to the values given in reference 7c, in order to be consistent with the definition in this work. $^d$ Data from reference 1. $^e$ Data from reference 6b. $^f$ mnt = maleonitriledithiolate, dmit = dimercaptoisotrithione, dtc = diethyldithiocarbamate.

symmetry. The restrictions of the tridentate [9]aneS$_3$ ligands are such that the axial S-donor atoms do not lie on the normal to the AuS$_4$ plane, and the S(axial)···Au···S(axial) vector is at an angle of 12.2° to this normal, which results in a shift of both of these axial donor atoms into the *yz* plane. This could give rise to a significant ligand contribution to the rhombicity and could perturb the overlap between the axial lone-pair S 3p orbitals with the Au 5d$_{xz}$ and 5d$_{yz}$ orbitals to produce a metal valence contribution to the in-plane anisotropy. However, the Mulliken population analysis based on the DFT results (Table 1) show no difference in the population of these two orbitals, which suggests that the ligand contribution dominates.

This distortion may also explain why the angle of twist ($\rho = 15°$) of the *P* tensor with respect to the *g* and *A* matrices about the *x*-axis was necessary to simulate the EPR spectra. The orientation of the principal axes of the *g* and *A* matrices are dictated by the distribution of the electron *spin* density, and the SOMO of [Au([9]aneS$_3$)$_2$]$^{2+}$ is an in-plane orbital with 5d$_{xy}$ being the major metal component. Thus, we expect $g_{zz}$ and $A_{zz}$ to be normal to the *xy* plane. In contrast, the principal axes of the *P* tensor are dictated by the *total* electron (charge) density distribution. Whereas in a square planar complex $P_{zz}$, the largest element of the *P* tensor, would also be expected to be normal to the coordination plane, the two axial S-donors in [Au([9]-aneS$_3$)$_2$]$^{2+}$ will give rise to a significant EFG component along the S(axial)···Au···S(axial) vector. This could result in the *P* tensor rotating away from *g* and *A*, and indeed the angle of non-co-incidence of 15° is remarkably close to the angle between this vector and the normal to the equatorial AuS$_4$ plane (12.1°).

**Comparison of [Au([9]aneS$_3$)$_2$]$^{2+}$ with {Au(II)S$_4$} Species.** A summary of *g* values, $^{197}$Au *A* values, and *P* values for [Au([9]aneS$_3$)$_2$]$^{2+}$ are given in Table 2 together with those for other nominally Au(II), thio-ligand complexes for comparison, namely [Au(mnt)$_2$]$^{2-}$, [Au(dmit)$_2$]$^{2-}$, and [Au(dtc)$_2$]. All of these complexes have significantly delocalised ground states where the dominant metal component is 5d$_{xy}$. The latter three

There is a large rhombic anisotropy in the *xy* plane for the determined nuclear quadrupole parameters. With $P = \eta$, the quadrupole coupling, and therefore the EFG, is restricted to the *yz* plane. Although the simulations of the EPR spectra cannot assign the *x* and *y* axes, DFT calculations of the *g* matrix indicate that the smallest *g* value, $g_{yy}$, bisects approximately the in-plane S···Au···S chelate bite angles (87.7°) whereas $g_{xx}$ bisects approximately the non-chelate S···Au···S angles (92.3°) (Figure 5a). Very large rhombic asymmetries have also been observed in [Cu(mnt)$_2$]$^{2-}$ and [Au(mnt)$_2$]$^{2-}$.$^{2,47}$ For the Cu(II) complex, Belford argued that this rhombicity could either be due to the $\pi$-electron density localized on the C=C double bonds of the mnt$^{2-}$ ligands (a ligand, in-plane dipolar contribution to the EFG along one axis), or due to an imbalance of d$_{yz}$ and d$_{xz}$ net populations resulting from more efficient overlap of one of these orbitals with the $\pi$-systems of the chelating ligands (a metal valence contribution).$^{47}$ In the case of [Au([9]aneS$_3$)$_2$]$^{2+}$, the two axial S-donor atoms are at 2.839 Å from Au in a Jahn−Teller elongation, with the four equatorial S donors at 2.452 and 2.462 Å and lying in a perfect plane due to the $C_i$ point
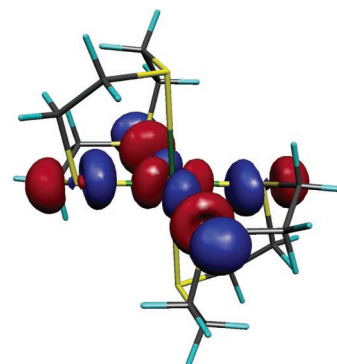
**Figure 6.** Coordinate frames and atom numbering schemes employed in the DFT calculations for (a) $[Au([9]aneS_3)_2]^{2+}$ and (b) $[Ag([18]aneS_6)]^{2+}$ in $C_i$ symmetry.



**Figure 7.** Isosurface plot of the α-spin SOMO of $[Au([9]aneS_3)_2]^{2+}$ derived from a BP-TZ2P all electron SR DFT calculation.

**Table 3.** Experimental and Calculated $g$ Matrix Components for $[Au([9]aneS_3)_2]^{2+}$

|  | exptl (EPR) | BP-TZP SO | BP-TZ2P SO | BP-TZP SO all electron | BP-TZ2P SO all electron |
|---|---|---|---|---|---|
| $g_1$ | 2.032 | 2.027 | 2.025 | 2.031 | 2.028 |
| $g_2$ | 1.999 | 2.004 | 2.004 | 2.001 | 2.001 |
| $g_3$ | 1.984 | 1.982 | 1.984 | 1.967 | 1.970 |
| $\Delta g_1$ | 30 | 25 | 23 | 29 | 26 |
| $\Delta g_2$ | −3 | 2 | 2 | −1 | −1 |
| $\Delta g_3$ | −18 | −20 | −18 | −35 | −32 |

complexes all give rather similar spin-Hamiltonian parameters. In comparison, $[Au([9]aneS_3)_2]^{2+}$ has larger hyperfine couplings and hyperfine anisotropy implying a greater d-orbital occupancy in the SOMO, i.e., greater Au(II)-like character. However, the quadrupole couplings for $[Au([9]aneS_3)_2]^{2+}$ are much smaller, by a factor of *ca.* 2. This is inconsistent with the changes in $a^2$ and, therefore, must be due to the changes in the nature of the ligands. There are several possible explanations for this: (a) replacing neutral $[9]aneS_3$ ligands with dianionic $mnt^{2-}$ (or $dmit^{2-}$ or $dtc^-$) will give rise to much greater EFGs along $z$ in the $mnt^{2-}$ complex; (b) the in-plane Au...S distances are considerably longer in the $[9]aneS_3$ complex, reducing the EFG; (c) in $mnt^{2-}$, there are delocalised π electrons (on the ethene bond) increasing the EFG. Belford has observed that on coordination of axial solvate ligands in square planar O- and S-donor Cu(II) complexes (changing from 4- to 6-coordinate), there is an increase in the EFG along the $z$-axis.[45] Thus, we might expect a slightly increased contribution to the EFG in our system from the coordination of the two axial S-donor atoms. However, comparison with $[Au(mnt)_2]^{2-}$ indicates that the differences in the nature of the ligands in this case are far more important than the difference in coordination number in determining the EFG at Au.

**DFT Calculations on $[Au([9]aneS_3)_2]^{2+}$.** The experimental and calculated structural parameters for the $AuS_6$ coordination sphere in $[Au([9]aneS_3)_2]^{2+}$ were compared (see Supporting Information), and the atom-numbering scheme and coordinate frame employed in the calculations are shown in Figure 6. The $y$ axis bisects the $S(1)-Au-S(2)$ angle and the $x$ axis also lies in the equatorial $AuS_4$ plane. The ZORA SR DFT calculations reveal tetragonally elongated stereochemistries for $[Au([9]-aneS_3)_2]^{2+}$ that are consistent with a $d^9$ Jahn–Teller distorted Au(II) center. For the frozen core TZP basis set, the calculated

$Au-S(1)/S(2)$ and $Au-S(3)$ distances are longer by *ca.* 0.09 and 0.15 Å, respectively, and the $S-Au-S$ bond angles are *ca.* 2° smaller than those observed in the X-ray crystal structure of $[Au([9]aneS_3)_2](BF_4)_2$. Nevertheless, the relative differences in Au–S bond lengths within the calculated and experimental geometries are similar (*ca.* 0.01 and *ca.* 0.38−0.44 Å between the equatorial Au–S bond distances, and between the axial Au–S and equatorial Au–S bond distances, respectively). Thus, the overall similarities between the calculated and experimental geometries for $[Au([9]aneS_3)_2]^{2+}$ suggest that these DFT calculations are of sufficient quality to permit a qualitative understanding of the electronic properties of $[Au([9]aneS_3)_2]^{2+}$. The inclusion of all electrons in the TZP basis set and the enlargement of the Au basis to TZ2P does not substantially improve the agreement between the calculated and experimental structures of $[Au([9]aneS_3)_2]^{2+}$.

The calculated SOMO for $[Au([9]aneS_3)_2]^{2+}$ (Figure 7), using a TZ2P all electron basis set for Au and a TZP all electron basis set for all other atoms, is composed of 27.7% Au $5d_{xy}$ and 62.8% equatorial S $3p$ character. This overall description remains essentially unchanged for calculations employing all electron and frozen core TZP and TZ2P basis sets.

A comparison between the experimental and calculated $g$ matrix components is presented in Table 3. Calculations using the ZORA SO formalism with a frozen core TZP basis set yield $g$ matrix components that deviate from the experimental values by −5, 5, and −2 ppt for $g_1$, $g_2$, and $g_3$, respectively. The use of all electron basis sets and/or the use of a TZ2P basis set for Au does not significantly improve the correspondence between the experimental and calculated values. Similar deviations between experimental and calculated $g$ matrix components have been reported previously and have been ascribed to over- and under-estimations in the contributions from the second-order spin−orbit/orbital term in the calculated $g$ matrix.[49−52] Furthermore, the relative insensitivity of the calculated $g$ matrix with the treatment of the core electrons within the basis set reflects
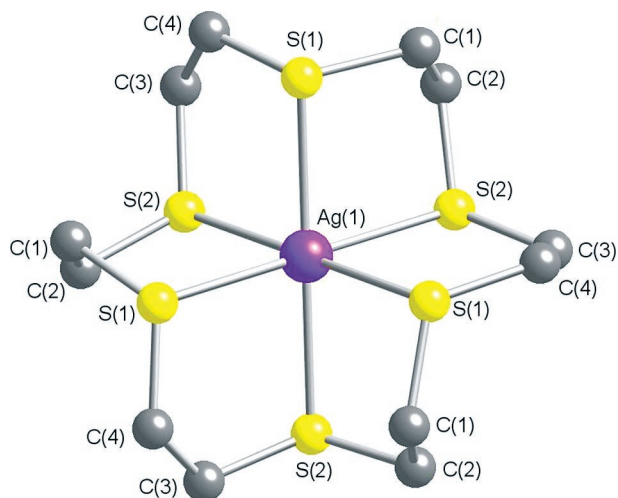
**Figure 8.** Structure of [Ag([18]aneS$_6$)](ClO$_4$)$_2$ at 30 K with minor disorder component of C1, C2 omitted.

the fact that the *g* matrix is a property principally of the valence electrons. Thus, the reproduction of the trends in the metrical parameters for the AuS$_6$ coordination sphere, the agreement between the calculated and EPR-derived Au contribution to the SOMO and the smaller deviations between the calculated and experimental *g* matrix components support a SOMO in [Au-([9]aneS$_3$)$_2$]$^{2+}$ that possesses *ca.* 30% Au 5d$_{xy}$ character. The calculated orientation of the principal *g* values with respect to the molecular frame is shown in Figure 5a. The largest principal *g* value ($g_1$) is approximately perpendicular to the *xy* plane, as expected for a formal d$_{xy}$ SOMO, and lies 7.9° off the *z*-axis which is perpendicular to the AuS$_4$ plane. The remaining principal *g* values, $g_2$ and $g_3$, are 2.2 and 7.6° away from the *x* and *y* axes, respectively.

**Synthesis and Characterization of [Ag([18]aneS$_6$)]ClO$_4$ and [Ag([18]aneS$_6$)](ClO$_4$)$_2$.** [Ag([18]aneS$_6$)]ClO$_4$ was prepared via reaction of a solution of AgClO$_4$ and 1 equiv of [18]aneS$_6$ in MeNO$_2$ under reflux and an inert atmosphere in the absence of light for 30 min.[38,39] The resulting solution was filtered through Keiselghur, and Et$_2$O was added to the filtrate with vigorous stirring. [Ag([18]aneS$_6$)]ClO$_4$ was isolated as a white solid and collected by filtration. HClO$_4$ (70%) was added to a MeCN solution of [Ag([18]aneS$_6$)]ClO$_4$, and a color change from colorless to deep royal blue was observed. [Ag([18]aneS$_6$)]-(ClO$_4$)$_2$ was collected by filtration as a deep-royal-blue solid. Needles of [Ag([18]aneS$_6$)](ClO$_4$)$_2$ were grown by slow diffusion of HClO$_4$ (70%) through an aqueous slurry of silica gel into a solution of [Ag([18]aneS$_6$)]ClO$_4$ in MeNO$_2$.

**Crystal Structure Determination of [Ag([18]aneS$_6$)]-(ClO$_4$)$_2$.** [Ag([18]aneS$_6$)](ClO$_4$)$_2$ has been structurally characterized by single-crystal X-ray diffraction at 150 and 30 K and is the first structurally characterized Ag(II) complex with homoleptic thioether S-donor ligation. The single-crystal X-ray structure of [Ag([18]aneS$_6$)](ClO$_4$)$_2$ confirms octahedral homoleptic thioether coordination (Figure 8). At 150 K, the structure
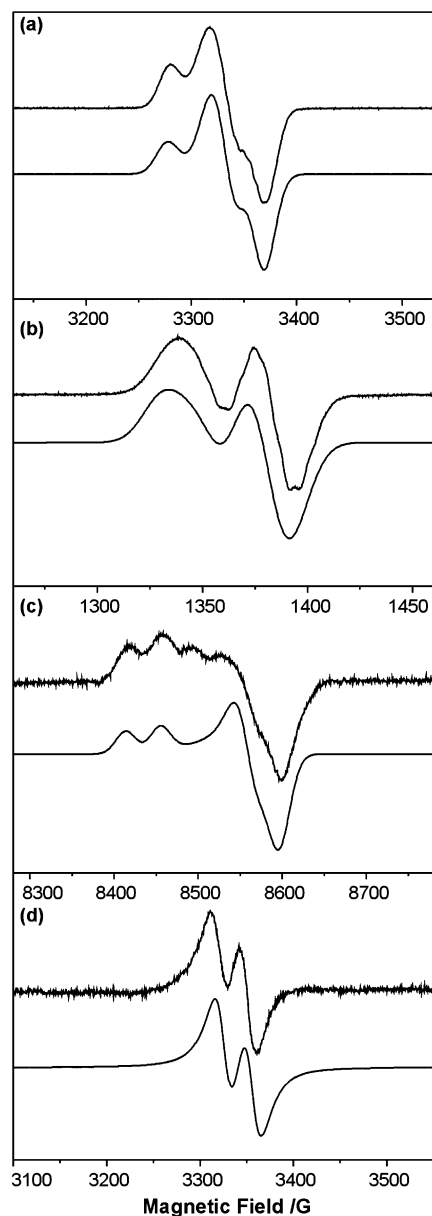
(48) Kaupp, M.; Reviakine, R.; Malkina, O. L.; Arbuznikov, A.; Schimmelpfennig, B.; Malkin, V. G. *J. Comput. Chem.* **2002**, *23*, 794−803.
(49) Patchkovskii, S.; Ziegler, T. *J. Chem. Phys.* **1999**, *111*, 5730−5740.
(50) Patchkovskii, S.; Ziegler, T. *J. Am. Chem. Soc.* **2000**, *122*, 3506−3516.
(51) van Lenthe, E.; van der Avoird, A.; Hagen, W. R.; Reijerse, E. J. *J. Phys. Chem. A* **2000**, *104*, 2070−2077.
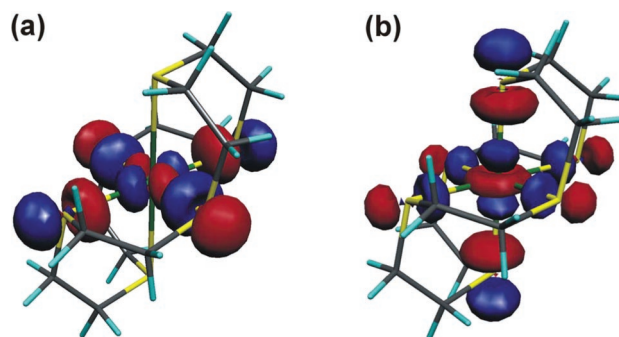(52) Stein, M.; van Lenthe, E.; Baerends, E. J.; Lubitz, W. *J. Phys. Chem. A* **2001**, *105*, 416−425.

contains two independent Ag(II)−S distances of 2.569(7) and 2.720(6) Å. However, the three-fold symmetry of the complex means that there are three of each distance. These distances are shorter than those in the structure of the tetragonally compressed [Ag([18]aneS$_6$)]$^+$ where the two axial bond lengths are 2.6665(12) Å and the four equatorial bond lengths are 2.7813(10) Å.[38,39] At 30 K, the structure still contains two independent Ag(II)−S distances of 2.615(6) and 2.620(6) Å. However, these bond lengths exhibit greater similarity than those measured at 150 K and, as well as being equivalent, there are still three of each distance due to the three-fold symmetry of the complex, suggesting that even at 30 K there is some disorder of the axis of elongation.

**Multi-Frequency EPR Studies on [Ag([18]aneS$_6$)]$^{2+}$.** [Ag([18]aneS$_6$)]$^{2+}$ was studied in H$_2$SO$_4$ solution as a fluid at X-band, and as a frozen solution at S-, X-, and K-band. The fluid solution X-band spectrum at room temperature (Figure 9d) is a simple doublet arising from hyperfine coupling of the unpaired electron to the $^{107,109}$Ag nucleus (both $I$ = 1/2, 100% combined natural abundance). Simulation gives the isotropic parameters $g_{iso}$ = 2.019, $A_{iso}$ = +28 × 10$^{-4}$ cm$^{-1}$. On freezing this solution at *ca.* 110 K, the X-band spectrum (Figure 9a) appears axial with overlapping parallel and perpendicular components ($g_{||}$ > $g_{\perp}$), both of which show coupling to Ag. There is also partial resolution of hyperfine coupling to ligand nuclei on the perpendicular feature, which is better resolved at S-band (Figure 9b; splitting *ca.* 7 G) at the expense of much poorer *g* resolution. At K-band, the parallel Ag hyperfine doublet is clearly resolved at the low-field end of the spectrum, while the shoulder in the perpendicular feature is due to partial resolution of the Ag hyperfine doublet. The spectra, across all frequencies, are best simulated assuming a simple axial system with $g_{zz}$ = 2.046, $g_{xx}$ = $g_{yy}$ = 2.013, and hyperfine coupling to Ag with $A_{zz}$ = +38 × 10$^{-4}$ cm$^{-1}$, $A_{xx}$ = $A_{yy}$ = +23 × 10$^{-4}$ cm$^{-1}$. There is an additional feature in the middle of the K-band spectrum (Figure 9c) at *ca.* 8500 G that is not simulated with this model, and is likely due to an impurity. We have not attempted to reproduce the superhyperfine structure in the perpendicular features of the lower frequency spectra, but this is most likely due to ligand protons.

**Interpretation of EPR Data for [Ag([18]aneS$_6$)]$^{2+}$.** In a simple crystal field model assuming a Ag(II), 4d$^9$ configuration, we would expect the unpaired electron to be in the 4d$_{xy}$ orbital. In this case, the principal components of the *g* and *A* matrices are given by eqs 1 and 2,[41] respectively, where $P_d$ is now the electron−nuclear dipolar coupling parameter for Ag 4d electrons, and *a* is the LCAO coefficient of the Ag 4d$_{xy}$ orbital in the SOMO. The experimental *g* and metal *A* values for [Ag([18]aneS$_6$)]$^{2+}$ are consistent with eqs 1 and 2. The *g* values are all greater than $g_e$, with $g_{zz}$ being associated with the largest principal hyperfine value $A_{zz}$ and oriented perpendicular to the plane of the 4d$_{xy}$ orbital. The experimental *A* values must all be the same sign as each other and as $A_{iso}$, because the anisotropic values average well to $A_{iso}$. From eq 4 and the assignment above, we can calculate $a^2$, the spin density in the Ag 4d$_{xy}$ orbital (or the admixture of 4d$_{xy}$ to the SOMO), without the need to explicitly assign *x* and *y*. We have calculated $P_d$ for $^{107}$Ag for the possible electronic configurations 4d,$^8$ 4d$^9$, and 4d$^8$6s$^1$ using Rieger's methodology,[44] as −80.1 × 10$^{-4}$, −74.7 × 10$^{-4}$ and −79.1 × 10$^{-4}$ cm$^{-1}$, respectively. Substitution of the experi-

**Figure 10.** Isosurface plots of the α-spin SOMO of $[Ag([18]aneS_6)]^{2+}$ derived from BP-TZ2P all electron SR DFT calculations on (a) geometry **1** and (b) geometry **2**.

employing starting geometries with axial elongation and equatorial compression (geometry **1**), and axial compression and equatorial elongation (geometry **2**) were performed to facilitate convergence and to assess the extent of distortion within the $AgS_6$ coordination sphere that may not be resolved by X-ray crystallography. The calculated structural parameters for the $AgS_6$ coordination sphere for $[Ag([18]aneS_6]^{2+}$ geometries **1** and **2** were compared (Supporting Information), and the atom numbering scheme employed in the calculations is shown in Figure 6b.

Models employing starting geometries **1** and **2** result in geometry-optimized structures containing tetragonally elongated (for geometry **1**) and compressed (for geometry **2**) $AgS_6$ centers that are consistent with a $d^9$ Jahn−Teller distorted Ag(II) center. The average calculated Ag−S distances for the geometry-optimized structures vary little with the choice of basis set and lie within $3\sigma$ of the Ag−S distances obtained from X-ray crystallography. The geometry-optimized structures differ by *ca.* 0.2 kcal mol$^{-1}$ (70 cm$^{-1}$) for identical model chemistries, which may indicate plasticity in the $AgS_6$ coordination sphere that manifests in axial and equatorial Ag−S distances that are not resolved from one another by X-ray crystallography. The calculated SOMO for $[Ag([18]aneS_6)]^{2+}$ (Figure 10a), using a TZ2P all electron basis set for Ag and geometry **1** as the initial coordinates is composed of 22.0% Ag $4d_{xy}$ and 65.6% equatorial S 3p character. For geometry **2** the nature of the calculated SOMO switches (Figure 10b) to a 20.1% Ag $4d_{z^2}$ and 67.9% S 3p composition for a TZ2P all electron basis set for Ag. These overall descriptions of the SOMOs for the calculated structures derived from geometries **1** and **2** remain unchanged for calculations employing frozen core TZP and TZ2P basis sets. A comparison between the experimental and calculated *g* matrix. components is presented in Table 4. The experimental EPR spectra may be simulated with axial spin-Hamiltonian parameters at all frequencies with $g_{zz} > g_{xx,yy}$. For geometry **1**, the calculated principal *g* values exhibit a rhombic pattern that increases in rhombicity for calculations employing all electron basis sets. The calculated $g_1$ value (2.035) with a TZ2P all-electron basis set is 11 ppt lower than the experimental $g_{zz}$ value (2.0046). The calculated $g_2$ and $g_{xx}$ values compare well with one another ($g_2$ =2.011 and $g_{xx}$ =2.013) and $g_3$ (1.979) is 34 ppt lower than the experimental $g_{yy}$ (2.013) value. The orientation of the calculated principal *g* values with respect to the molecular frame is shown in Figure 5b for calculations employing an all-electron TZ2P basis set for Ag in geometry **1**. The $g_3$ principal g-value is essentially co-incident with the *y* axis and



**Figure 9.** EPR spectra of $[Ag([18]aneS_6)]^{2+}$ in $H_2SO_4$ at *ca.* 110 K (top) and simulation (below) (a) X-band, (b) S-band, and (c) K-band with $g_{zz}$ = 2.046, $g_{xx} = g_{yy}$ = 2.013, $A_{zz(Ag)}$ = 40 G, $A_{xx(Ag)} = A_{yy(Ag)}$ = 25 G with Gaussian linewidths of $W_{zz}$ = 18, $W_{xx} = W_{yy}$ = 21 G (S-band); $W_{zz}$ = 21, $W_{xx} = W_{yy}$ = 23 G (X-band); $W_{zz}$ = 23, $W_{xx} = W_{yy}$ = 27 G (K-band). (d) Room temperature, fluid solution X-band spectrum of $[Ag([18]aneS_6)]^{2+}$ in $H_2SO_4$ (top) and simulation below with $g_{iso}$ = 2.019, $A_{iso(Ag)}$ = 30 × 10$^{-4}$ cm$^{-1}$ with a Lorentzian linewidth of 21 G.

mental *g* and *A* values into eq 4 (assuming positive values of $A_{ii}$) gives $a^2$ = 0.26, 0.27 and 0.26, respectively. Negative values of $A_{ii}$ give negative values of $a^2$ which are nonsensical. Thus, the metal d-orbital contribution to the SOMO is *ca.* 26%.

**Geometry Optimization and SOMO Details for $[Ag([18]aneS_6)]^{2+}$.** The X-ray crystal structure of $[Ag([18]aneS_6)](ClO_4)_2$ at 150 and 30 K reveal a $AgS_6$ coordination sphere with three-fold symmetry defined by two Ag−S distances at each temperature [Ag(1)−S(1) = 2.615(6) Å and Ag(1)−S(2) = 2.620(6) Å at 30 K and Ag(1)−S(1) = 2.720(6) Å and Ag(1)−S(2) = 2.569(7) Å at 150 K]. DFT geometry-optimization calculations employing these geometries as the initial coordinates lead to SCF calculations that did not converge. Thus, calculations

**Table 4.** Experimental and Calculated *g*-Matrix Components for $[Ag[18]aneS_6]^{2+}$

| | experimental | BP-TZP SO | BP-TZ2P SO | BP-TZP SO | BP-TZ2P SO all electron |
|---|---|---|---|---|---|
| | | | geometry **1** | | |
| $g_1$ | 2.046 | 2.024 | 2.024 | 2.035 | 2.035 |
| $g_2$ | 2.013 | 2.010 | 2.010 | 2.011 | 2.011 |
| $g_3$ | 2.013 | 1.988 | 1.992 | 1.979 | 1.979 |
| $\Delta g_1$ | 41 | 22 | 22 | 33 | 33 |
| $\Delta g_2$ | 11 | 8 | 8 | 9 | 9 |
| $\Delta g_3$ | 11 | −14 | −10 | −23 | −23 |
| | | | geometry **2** | | |
| $g_1$ | 2.046 | 2.029 | 2.029 | 2.029 | 2.028 |
| $g_2$ | 2.013 | 2.026 | 2.027 | 2.026 | 2.026 |
| $g_3$ | 2.013 | 1.978 | 1.981 | 1.978 | 1.980 |
| $\Delta g_1$ | 41 | 27 | 27 | 27 | 26 |
| $\Delta g_2$ | 11 | 24 | 25 | 24 | 24 |
| $\Delta g_3$ | 11 | −24 | −21 | −24 | −24 |

$g_1$ and $g_2$ are rotated away from the *z* and *x* axes respectively by a rotation about the $g_3$/*y* axis of 12.1°. Calculations of the *g* matrix of geometry **2** yield *g* matrices that are axial and show much less variation with basis set than similar calculations on geometry **1** and with calculated principal *g* values and orientations that match a $g_{xx,yy} > g_{zz}$ pattern consistent with the formal $4d_{z^2}$ SOMO calculated for geometry **2**, but inconsistent with the EPR data for $[Ag([18]aneS_6)]^{2+}$.

Thus, the experimental spin Hamiltonian parameters $g_{zz} > g_{xx,yy}$ and the experimentally determined SOMO with *ca.* 26% Ag $4d_{xy}$ character are more consistent with the electronic structure calculated for geometry **1** than for that calculated for geometry **2** and suggest that in solution $[Ag([18]aneS_6)]^{2+}$ may exist in an axially elongated $AgS_6$ geometry.

## Summary

The electronic structures of the complexes $[Au([9]aneS_3)_2]^{2+}$ and $[Ag([18]aneS_6)]^{2+}$ have been elucidated. Results from the DFT calculations and detailed and comprehensive EPR simulations are in agreement and show that for $[Au([9]aneS_3)_2]^{2+}$, the SOMO has *ca.* 27−30% Au $5d_{xy}$ character and 62−63% equatorial S 3p character, thus confirming the non-innocence of thioether ligands in this system. $[Ag([18]aneS_6)]^{2+}$ has been structurally characterized; this is the first Ag(II) complex with homoleptic thioether coordination to be characterized by single-crystal diffraction. Spectroscopic and computational results are in agreement and show that the unpaired electron density is *ca.* 22−26% in the Ag $4d_{xy}$ orbital. Stace and co-workers have identified[53] from gas-phase studies that σ-donor and π-acceptor ligands are capable of stabilizing the M(II) (M = Cu, Ag, Au) oxidation states, although they identified that the stabilization of Ag(II) and Au(II) was more difficult. This is consistent with our own observations that metal-bound thioether crowns can behave potentially as both π-donors by donation of the remaining lone pair[33a] or as π-acceptor species.[54] The macrocyclic nature of the ligands used in the present study clearly enhance the stability of M(II) species. Thus, $[Ag([18]aneS_6)]^{2+}$ is stable over a few hours but only under acidic conditions (HClO₄), which minimizes decomposition via ring-opening β-elimination reactions.[33e] In contrast, $[Au([9]aneS_3)_2]^{2+}$ is an

air-stable solid that slowly decomposes in solution over 2 h at room temperature. The stereochemical flexibility and ambivalence of the crown ligands and their encapsulation of metal radical ions by polarizabale S-donors is, we believe, the basis of the stabilization of these unusual oxidation state species. Current work seeks to establish further the electronic structures of these unusual oxidation state species by MCD coupled to electronic and EPR spectroscopy.

## Experimental Section

**Computational Details.** The calculations were performed using the Amsterdam Density Functional (ADF) suite version 2003.01.[55] The unrestricted and restricted relativistic DFT calculations employed a Slater-type orbital (STO) triple-ζ-plus one polarization function basis set from the ZORA/TZP database of the ADF suite for all atoms except Au and Ag. All electron and frozen core basis sets (up to and including 2p for S, and 1s for C) were employed. For Au and Ag, triple-ζ-plus one polarization function (ZORA/TZP) and triple-ζ-plus two polarization functions (ZORA/TZ2P) all electron and frozen core basis sets (up to and including 4d and 3d for Au and Ag, respectively) were employed. Scalar relativistic (SR) and spin−orbit coupling (SO) approaches were used within the ZORA Hamiltonian for the inclusion of relativistic effects. The local density approximation (LDA) with the correlation potential due to Vosko *et al.*[56] was used in all of the DFT calculations. Gradient corrections were performed using the functionals of Becke[57] and Perdew (BP).[58] Models of $[Au([9]aneS_3)_2]^{2+}$ and $[Ag([18]aneS_6)]^{2+}$ in $C_i$ symmetry were constructed using geometrical data from the X-ray crystal structures of $[Au([9]aneS_3)_2](BF_4)_2$ and $[Ag([18]aneS_6)](ClO_4)_2$. The atom numbering schemes and the coordinate frames employed in the calculations are shown in Figure 6. The *y*-axis bisects the S(1)−M−S(2) angle in both structures and the *x*-axis lies in the equatorial $MS_4$ plane. The model geometries were optimized at the ZORA SR level. The *g* matrices were obtained from unrestricted ZORA SO calculations using the collinear approximation on the geometry optimized structures derived from unrestricted ZORA SR calculations with identical basis sets.

**Chemicals.** All chemicals were purchased from Aldrich, except hydrogen tetrachloroaurate (Alfa Aesar) and perchloric acid (Lancaster), and were used as received.

**Physical Measurements.** Multifrequency EPR spectra were recorded on a Bruker ESP 300E spectrometer. Simulations were performed using the commercial XSophe software.[59] Infrared spectra were recorded on a Nicolet Avatar 360 FTIR spectrometer. Mass spectra were obtained from the EPSRC National Mass Spectrometry Service center at the University of Wales, Swansea, UK. Elemental analyses were carried out by the Microanalytical Service at the University of Nottingham with an Exeter Analytical Inc CE-440 Elemental analyzer.

**$[Au([9]aneS_3)_2](BF_4)_2$.** In the absence of light, hydrogen tetrachloroaurate (67 mg, 0.19 mmol) was added to a stirring mixture of $[9]aneS_3$ (71 mg, 0.39 mmol) and 40% aqueous tetrafluoroboric acid (15 cm³) and heated under reflux for 15 min. MeNO₂ (40 cm³) and water (80 cm³) were added. The aqueous layer was washed with MeNO₂ (4 × 10 cm³), and the organics were combined and dried over MgSO₄ before the solvent was removed under reduced pressure. The resulting brown oil was washed with CH₂Cl₂. Yield: 54 mg (42%) Found: C 19.13, H 3.09 ($AuC_{12}H_{24}S_6B_2F_8$ requires: C 19.71, H 3.31); IR (KBr)

(53) Walker, N. R.; Wright, R. R.; Barran, P. E.; Murrell, J. N.; Stace, A. J. *J. Am. Chem. Soc.* **2001**, *123*, 4223−4227 and references therein.
(54) Blake, A. J.; Holder, A. J.; Hyde, T. I.; Schröder, M. *J. Chem. Soc. Chem. Commun.* **1989**, 1433−1434.

(55) (a) SCM, Vrije Universiteit Amsterdam; http://www.scm.com, Amsterdam, The Netherlands. (b) Guerra, C. F.; Snijders, J. G.; te Velde, G.; Baerends, E. J. *Theor. Chem. Acc.* **1998**, *99*, 391−403. (c) te Velde, G.; Bickelhaupt, F. M.; van Gisbergen, S. J. A.; Guerra, C. F.; Baerends, E. J.; Snijders, J. G.; Ziegler, T. *J. Comput. Chem.* **2001**, *22*, 931−967.
(56) Vosko, S. H.; Wilk, L.; Nusair, M. *Can. J. Phys.* **1980**, *58*, 1200−1211.
(57) Becke, A. D. *Phys. Rev. A: At., Mol., Opt. Phys.* **1988**, *38*, 3098−3100.
(58) Perdew, J. P. *Phys. Rev. B: Condens. Matter Mater. Phys.* **1986**, *33*, 8822−8824.
(59) *XSophe Computer Simulation Suite*, Sophe version 1.1.3; University of Queensland: Australia and Bruker Biospin GmbH: Germany, 2003.

$\bar{\nu}_{max}/cm^{-1}$: 3413 b (O−H stretch), 2925 m (C−H stretch), 2897 m (C−H stretch), 1633 w, 1460 w, 1407 m, 1301 m, 1034 s (B−F stretch), 824 m, 533 m (B−F stretch); MS $m/z$: 577 (96%, $[M]^+$), 381 (5%, $[M − Au]^+$).

CARE: *Perchlorate salts may be explosive. Care was taken in the synthesis of the perchlorate salts described below not to evaporate to dryness or heat any solid formed. Perchlorate salts can also be shock sensitive.*

**[Ag([18]aneS$_6$)]ClO$_4$.** Under a nitrogen atmosphere and protected from light, a mixture of [18]aneS$_6$ (36 mg, 0.1 mmol) and silver perchlorate (21 mg, 0.10 mmol) in MeNO$_2$ (5 cm$^3$) was heated under reflux for 15 min. The colorless solution was filtered through Kieselghur before diethyl ether (20 cm$^3$) was added with vigorous stirring to give the product as a colorless precipitate, which was filtered and washed with diethyl ether and CH$_2$Cl$_2$. Yield: 48 mg (84%) Found: C 24.73, H 4.12 (AgC$_{12}$H$_{24}$S$_6$ClO$_4$ requires: C 25.37, H 4.26); IR (KBr) $\bar{\nu}_{max}/cm^{-1}$: 2975 m (CH stretch), 2920 m (C−H stretch), 1626 w, 1533 w, 1421 s, 1264 s, 1089 s (Cl−O stretch), 931 s, 622 s (Cl−O stretch); $^1$H NMR (CDCl$_3$) $\delta$/ppm: 2.98 (s); MS $m/z$: 469 (97%, $[M]^+$), 467 (100%, $[M]^+$).

**[Ag([18]aneS$_6$)]ClO$_4$.** A solution of [Ag([18]aneS$_6$)][ClO$_4$] (40 mg, 0.06 mmol) in MeCN (5 cm$^3$) was treated with 70% aqueous perchloric acid (*ca*. 5 cm$^3$) to give a royal-blue solution. A royal-blue solid precipitated from the solution after several hours. Yield: 34 mg (77%); IR (KBr) $\bar{\nu}_{max}/cm^{-1}$: 3380 b (O−H stretch), 2912 m (C−H stretch), 1424 m, 1088 s (Cl−O stretch), 940 m, 625 s (Cl−O stretch); MS $m/z$: 469 (94%, $[M]^+$), 467 (100%, $[M]^+$).

**Crystal Structure Determination of [Ag([18]aneS$_6$)](ClO$_4$)$_2$.** Royal-blue needles of [Ag[18]aneS$_6$](ClO$_4$)$_2$ suitable for study by X-ray diffraction were grown by slow diffusion of HClO$_4$ (70%) through an aqueous slurry of silica gel into a MeNO$_2$ solution of [Ag([18]aneS$_6$)]-ClO$_4$.

**150 K Refinement.** C$_{12}$H$_{24}$AgCl$_2$O$_8$S$_6$, MW 667.44, trigonal, space group $P3$, purple needle with dimensions $0.39 \times 0.01 \times 0.01$ mm$^3$ mounted in Fomblin film, $a = 10.973(2)$ Å, $c = 5.230(2)$ Å, $T = 150$ K, $Z = 1$, $R_1 = 0.072$ for 1202 reflections with $I > 2\sigma(I)$ and $wR_2 = 0.076$ for all 1250 reflections, GOF = 1.20. Single-crystal X-ray diffraction data were collected on a Bruker APEX diffractometer equipped with an Oxford Cryosystems Cryostream N$_2$ flow cryostat. Disorder in one C$_2$H$_4$ bridge is modeled as two half-occupied sites. The oxygen atoms of one ClO$_4^-$ anion are also disordered with one modeled over three 0.333 occupied sites around the three-fold axis and the other independent O atom for this anion modeled over two sites with occupancies 0.667 and 0.333. Disordered atoms were modeled with isotropic adps and distance restraints.

**30 K refinement.** C$_{12}$H$_{24}$AgCl$_2$O$_8$S$_6$, MW 667.44, trigonal, space group $P3$, purple needle with dimensions $0.36 \times 0.01 \times 0.01$ mm$^3$ mounted in Fomblin film, $a = 10.851(2)$ Å, $c = 5.186(2)$ Å, $T = 30$ K, $Z = 1$, $R_1 = 0.041$ for 876 reflections with $I > 2\sigma(I)$ and $wR_2 = 0.092$ for all 1113 reflections, GOF = 0.094. Single-crystal X-ray diffraction data were collected on a Bruker APEX diffractometer equipped with a Bede Microsource and Oxford Cryosystems HELIX He flow cryostat. The crystal was cooled to and maintained at 30 K throughout data collection. The symmetry is close to that of space group $P\bar{3}$ but would require an unreasonable disorder model for the C$_2$H$_4$ bridge where two CH$_2$ groups would clash. The model in $P3$ consists of the Ag atom situated on a three-fold axis with two unique S atoms and two unique C$_2$H$_4$ groups, one of which is disordered over two half-occupied sites. Both perchlorate anions lie on three-fold axes.

**Supporting Information Available:** EPR spectra and data, tables of geometrical parameters and the composition of the SOMO for [Au([9]aneS$_3$)$_2$]$^{2+}$ and [Ag([18]aneS$_6$)]$^{2+}$, X-ray crystallographic files (CIF) with tables of bond lengths and angles for the structure of [Ag([18]aneS$_6$)](ClO$_4$)$_2$. This material is available free of charge via the Internet at http://pubs.acs.org.

JA0636439